to appear in the *Astrophysical Journal*

The Visual Orbit of the 1.1-day Spectroscopic Binary σ^2 Coronae Borealis from Interferometry at the CHARA Array

Deepak Raghavan[1,2], Harold A. McAlister[1], Guillermo Torres[3], David W. Latham[3], Brian D. Mason[4], Tabetha S. Boyajian[1], Ellyn K. Baines[1], Stephen J. Williams[1], Theo A. ten Brummelaar[5], Chris D. Farrington[5], Stephen T. Ridgway[6], Laszlo Sturmann[5], Judit Sturmann[5], Nils H. Turner[5]

ABSTRACT

We present an updated spectroscopic orbit and a new visual orbit for the double-lined spectroscopic binary σ^2 Coronae Borealis based on radial velocity measurements at the Oak Ridge Observatory in Harvard, Massachusetts and interferometric visibility measurements at the CHARA Array on Mount Wilson. σ^2 CrB is composed of two Sun-like stars of roughly equal mass in a circularized orbit with a period of 1.14 days. The long baselines of the CHARA Array have allowed us to resolve the visual orbit for this pair, the shortest period binary yet resolved interferometrically, enabling us to determine component masses of 1.137 $\pm$ 0.037 $M_\odot$ and 1.090 $\pm$ 0.036 $M_\odot$. We have also estimated absolute V-band magnitudes of $M_{\rm V}$(primary) = 4.35 ± 0.02 and $M_{\rm V}$(secondary) = 4.74 ± 0.02. A comparison with stellar evolution models indicates a relatively young age of 1–3 Gyr, consistent with the high Li abundance measured previously. This pair is the central component of a quintuple system, along with another similar-mass star, σ^1 CrB, in a $\sim$ 730-year visual orbit, and a distant M-dwarf binary, σ CrB C, at a projected separation of $\sim 10'$. We also present differential proper motion evidence to show that components C & D (ADS 9979C & D) listed for this

[1]Center for High Angular Resolution Astronomy, Georgia State University, P.O. Box 3969, Atlanta, GA 30302-3969

[2]raghavan@chara.gsu.edu

[3]Harvard-Smithsonian Center for Astrophysics, 60 Garden Street, Cambridge, MA 02138

[4]US Naval Observatory, 3450 Massachusetts Avenue NW, Washington DC 20392-5420

[5]The CHARA Array, Mount Wilson Observatory, Mount Wilson, CA 91023

[6]National Optical Astronomy Observatory, P.O. Box 26732, Tucson, AZ 85726-6732

system in the Washington Double Star Catalog are optical alignments that are not gravitationally bound to the σ CrB system.

Subject headings: binaries: spectroscopic - stars: fundamental parameters - stars: individual (σ^2 Coronae Borealis) - techniques: interferometric

1. Introduction

σ CrB is a hierarchical multiple system 22 pc away. Its primary components, σ^1 CrB (HR 6064; HD 146362) and σ^2 CrB (HR 6063; HD 146361), are in a visual orbit with a preliminary period of $\sim$ 900 years (Scardia 1979), of which the latter is an RS CVn binary with a circularized and synchronized orbit of 1.139-day period (Strassmeier & Rice 2003, SR03 hereafter). In addition to these three solar-type stars, the Washington Double Star Catalog[1] (WDS) lists three additional components for this system. WDS components C and D were resolved 18″ away at 103° in 1984 (Popović 1986) and 88″ away at 82° in 1996 (Courtot 1996), respectively. We will show in § 7 that both these components are optical alignments that are not gravitationally bound to the σ CrB system. Finally, WDS component E (σ CrB C, HIP 79551) which was resolved 635″ away at 241° in 1991 by *Hipparcos* (Perryman & ESA 1997), was identified as a photocentric-motion binary by Heintz (1990). The parallax and proper motion listed for this star in van Leeuwen (2007), the improved *Hipparcos* results based on a new reduction of the raw data, match the corresponding measures for σ^2 CrB within the errors, confirming a physical association.

SR03 presented photometric evidence in support of a rotation period of 1.157 ± 0.002 days for both components of σ^2 CrB, the central pair of this system. They explained the 0.017-day difference between the rotation and orbital periods as differential surface rotation. Bakos (1984) estimated an orbital inclination of 28°, assuming component masses of 1.2 $M_\odot$ based on spectral types. SR03 subsequently adopted this inclination to obtain component masses of 1.108 ± 0.004 $M_\odot$ and 1.080 ± 0.004 $M_\odot$, but these masses are based on circular reasoning, and the errors are underestimated as they ignore the uncertainty in inclination. Several spectroscopic orbits have been published for this pair (Harper 1925; Bakos 1984; Duquennoy & Mayor 1991; SR03), enabling the spectroscopic orbital elements to be well-constrained. We present an updated spectroscopic solution based on these prior data and our own radial velocity measurements (§ 2.1, § 4.1). Our visual orbit leverages these spectroscopic solutions and derives all orbital elements for this binary (§ 5), leading to

[1]http://ad.usno.navy.mil/wds/

accurate component masses (§ 6.1).

This work utilizes a very precise parallax measure for this radio-emitting binary obtained by Lestrade et al. (1999) using Very Long Baseline Interferometry (VLBI). Their parallax of 43.93 ± 0.10 mas is about 10 times more precise than the *Hipparcos* catalog value of 46.11 ± 0.98 mas and 12 times more precise than the van Leeuwen (2007) measure of 47.35 ± 1.20 mas. The Lestrade et al. value is 2.2-σ and 2.9-σ lower than the *Hipparcos* and van Leeuwen measures, respectively. To check for systematic offsets, we compared the parallaxes for all overlapping stars in these three sources. While the difference in parallax is most significant for σ^2 CrB, we found no systematic differences. Moreover, Lestrade et al. performed statistical checks to verify the accuracy of their measure, so we adopt their parallax to derive the physical parameters of the component stars (§ 6).

The Center for High Angular Resolution Astronomy (CHARA) Array's unique capabilities, facilitated by the world's longest optical interferometric baselines, have enabled a variety of astrophysical studies (e.g., McAlister et al. 2005; Baines et al. 2007; Monnier et al. 2007). This work utilizes the Array's longest baselines to resolve the 1.14-day spectroscopic binary, the shortest period system yet resolved. While this is the first visual orbit determined using interferometric visibilities measured with the CHARA Array, the technique described here has regularly been employed for longer-period binaries using other long-baseline interferometers (e.g., Hummel et al. 1993; Boden et al. 1999). The σ^2 CrB binary has a projected angular separation of about 1.1 mas in the sky, making it easily resolvable for the CHARA Array, which has angular resolution capabilities in the K' band down to about 0.4 mas for binaries.

2. Spectroscopic Measurements

Spectroscopic observations of σ^2 CrB were conducted at the Harvard-Smithsonian Center for Astrophysics (CfA) with an echelle spectrograph on the 1.5m Wyeth reflector at the Oak Ridge Observatory in the town of Harvard, Massachusetts. A total of 46 usable spectra were gathered from 1992 May to 1999 July, each of which covers a single echelle order (45 Å) centered at 5188.5 Å and was recorded using an intensified photon-counting Reticon detector (see Latham 1992). The strongest lines in this window are those of the Mg I b triplet. The resolving power of these observations is $\lambda/\Delta\lambda \approx 35{,}000$, and the nominal signal-to-noise ratios range from 21 to 94 per resolution element of 8.5 $\mathrm{km\,s^{-1}}$.

Radial velocities were obtained using the two-dimensional cross-correlation algorithm TODCOR (Zucker & Mazeh 1994). Templates for the cross correlations were selected from

an extensive library of calculated spectra based on model atmospheres by R. L. Kurucz[2] (see also Nordström et al. 1994; Latham et al. 2002). These calculated spectra cover a wide range of effective temperatures ($T_{\rm eff}$), rotational velocities ($v \sin i$ when seen in projection), surface gravities ($\log g$), and metallicities. Experience has shown that radial velocities are largely insensitive to the surface gravity and metallicity adopted for the templates. Consequently, the optimum template for each star was determined from extensive grids of cross-correlations varying the temperature and rotational velocity, seeking to maximize the average correlation weighted by the strength of each exposure. The results we obtain, adopting $\log g = 4.5$ and solar metallicity[3] for both stars, are $T_{\rm eff} = 6050$ K and $v \sin i = 26$ km s^{-1} for the primary, and $T_{\rm eff} = 5870$ K and $v \sin i = 26$ km s^{-1} for the secondary. Estimated uncertainties are 150 K and 1 km s^{-1} for the temperatures and projected rotational velocities, respectively. Template parameters near these values were selected for deriving the radial velocities. Typical uncertainties for the velocities are 1 km s^{-1} for both stars.

The stability of the zero-point of our velocity system was monitored by means of exposures of the dusk and dawn sky, and small run-to-run corrections were applied in the manner described by Latham (1992). Additional corrections for systematics were applied to the velocities as described by Latham et al. (1996) and Torres et al. (1997) to account for residual blending effects. These corrections are based on simulations with artificial composite spectra processed with TODCOR in the same way as the real spectra. The final heliocentric velocities and their 1-σ errors are listed in Table 1, along with the corresponding epochs of observation, $O-C$ residuals, and orbital phase.

The light ratio between the components was estimated directly from the spectra following Zucker & Mazeh (1994). After corrections for systematics analogous to those described above, we obtain $\ell_{\rm s}/\ell_{\rm p} = 0.67 \pm 0.02$ at the mean wavelength of our observations (5188.5 Å). Given that the stars have slightly different temperatures, a small correction to the visual band was determined from synthetic spectra integrated over the V passband and the spectral window of our observations. The corrected value is $(\ell_{\rm s}/\ell_{\rm p})_V = 0.70 \pm 0.02$.

The visual companion σ^1 CrB was also observed spectroscopically at the CfA with the

[2]Available at `http://cfaku5.cfa.harvard.edu`.

[3]SR03 have reported a metallicity for σ^2 CrB of [Fe/H] = −0.37 with an uncertainty no smaller than 0.1 dex, and Nordström et al. (2004) reported the value [Fe/H] = −0.24 based on Strömgren photometry. Metallicity determinations for double-lined spectroscopic binaries are particularly difficult, and both of these estimates are likely to be affected at some level by the double-lined nature of the system. However, the visual companion (σ^1 CrB) is apparently a single star, and has an accurate spectroscopic abundance determination by Valenti & Fischer (2005) giving [Fe/H] = -0.06 ± 0.03, and another by Fuhrmann (2004) giving [Fe/H] = -0.064 ± 0.068. The near-solar metallicity from these determinations is considered here to be more reliable.

same instrumental setup. We obtained 18 observations between 1996 June and 2004 August. The stellar parameters were determined with a procedure similar to that used for σ^2 CrB, and yielded $T_{\rm eff} = 5950 \pm 100$ K and $v \sin i = 3 \pm 2$ km s^{-1}, for an adopted $\log g = 4.5$ and solar metallicity (see Footnote 3). Radial velocities were obtained with standard cross-correlation techniques using a template selected according to the above parameters. These measurements give an average velocity of -14.70 ± 0.11 km s^{-1}, with no significant variation within the observational errors. We use this radial velocity to unambiguously determine the longitude of the ascending node for the wider $\sigma^1 - \sigma^2$ CrB visual orbit (§ 6.4).

2.1. Historical Data Sets

In addition to our own, four other radial-velocity data sets have been published in the literature (Harper 1925; Bakos 1984; Duquennoy & Mayor 1991; SR03). Except for the more recent one, the older data are generally of lower quality and contribute little to the mass determinations, but they do extend the time coverage considerably (to nearly 86 years, or 27,500 orbital cycles) and can be used to improve the orbital period. Because of our concerns over possible systematic differences among different data sets, particularly in the velocity semi-amplitudes but also in the velocity zero points, we did not simply merge all these observations together indiscriminately, but instead we proceeded as follows. We considered all observations simultaneously in a single least-squares orbital fit, imposing a common period and epoch of maximum primary velocity in a circular orbit, but we allowed each data set to have its own velocity semi-amplitudes ($K_{\rm p}$, $K_{\rm s}$) as well as its own systematic velocity zero-point offset relative to the reference frame defined by the CfA observations. Additionally, we included one more adjustable parameter per set to account for possible systematic differences between the primary and secondary velocities in each group. These were statistically significant only in the observations by SR03. Relative weights for each data set were determined by iterations from the RMS residual of the fit, separately for the primary and secondary velocities. The resulting orbital period is $P = 1.139791423 \pm 0.000000080$ days, and the time of maximum primary velocity nearest to the average date of the CfA observations is $T = 2{,}450{,}127.61845 \pm 0.00020$ (HJD). We adopt this ephemeris for the remainder of the paper.

3. Interferometric Measurements

Interferometric visibilities for σ^2 CrB were measured during 2007 May−July at the CHARA Array's six-element long-baseline interferometer located on Mount Wilson, Cali-

fornia (ten Brummelaar et al. 2005). The Array uses the visible wavelengths 480–800 nm for tracking and tip/tilt corrections, and the near-infrared K' (2.13 μm) and H (1.67 μm) bands for fringe detection. The 26 visibility measurements used in the final orbit determination, listed in Table 2, were obtained in the K' band on the S1-E1 and S1-E2 two-telescope baselines spanning projected baselines of 268–331 meters. The interference fringes were obtained using the pupil-plane "CHARA Classic" beam combiner. While some of the data were obtained via on-site observing at Mount Wilson, the bulk of the data were gathered at the Arrington Remote Operations Center (AROC, Fallon et al. 2003) located at the Georgia State University campus in Atlanta, Georgia. Following the standard practice of time-bracketed observations, we interleaved each target visibility measurement with those of a calibrator star (HD 152598) in order to remove instrumental and atmospheric effects. For further details on the observing practice and the data reduction process, refer to McAlister et al. (2005).

We selected HR 6279 (HD 152598), an F0V star offset from σ^2 CrB by 8.°3, as the calibrator based on its small estimated angular diameter and its apparent lack of any close companions. We obtained photometric measurements for this star in the Johnson UBV bands from Grenier et al. (1985) and Perryman & ESA (1997), and JHK_S bands from the Two Micron All Sky Survey[4] (2MASS) and transformed them to calibrated flux measurements using the methods described in Colina et al. (1996) and Cohen et al. (2003). We then fitted these fluxes to spectral energy distribution models[5], yielding an angular diameter of 0.467 ± 0.013 mas for HD 152598, corresponding to $T_{\rm eff} = 7150$ K and $\log g = 4.3$. This diameter estimate results in a predicted calibrator visibility of $V_{\rm cal} = 0.858 \pm 0.008$ at our longest baseline of 330 m, contributing roughly 1% error to the calibrated visibilities. This error is included in our roughly 10% total visibility errors listed in Table 2, along with the epoch of observation (at mid-exposure), the target star's calibrated visibility, the predicted visibility for the best-fit orbit, the $O-C$ visibility residual, the baseline projections along East-West (u) and North-South (v) directions, and the hour angle of the target.

4. Determination of the Orbit

Consistent with prior evidence of a synchronized orbit (SR03), we adopt a circular orbit ($e \equiv 0$, $\omega \equiv 0$) with the orbital period (P) and epoch of nodal passage (T) from § 2.1 for the spectroscopic and visual orbit solutions presented below.

---

[4]`http://www.ipac.caltech.edu/2mass`

[5]The model fluxes were interpolated from the grid of models from R. L. Kurucz, available at `http://cfaku5.cfa.harvard.edu`

4.1. Spectroscopic Orbital Solutions

Our measured radial velocities enable us to derive the three remaining spectroscopic orbital elements, namely, the center-of-mass velocity (γ) and the radial velocity semi-amplitudes of the primary and secondary ($K_{\rm p}$ and $K_{\rm s}$, respectively). To check for consistency with prior efforts, we used the velocities published in SR03 to derive a second orbital solution. The calculated radial velocities for the derived orbits are shown in Figures 1 and 2 (solid and dashed curves for the primary and secondary, respectively) along with the measured radial velocities and residuals for the primary (filled circles) and secondary (open circles). The corresponding orbital solutions are presented in Table 3 along with the related derived quantities. For comparison purposes, we have also included the values presented in SR03, which are consistent with our orbit generated using their velocities. However, the orbit obtained using our velocities is statistically different from the one obtained using SR03 velocities. While the primary's velocity semi-amplitude matches within the errors between these two solutions, the secondary's differs by over 5-σ, resulting in a 4-σ difference in the mass ratios.

One possible explanation of the difference in the orbital solutions could be the velocity residuals for the orbit using SR03 data (Figure 2), which show an obvious pattern for both components. Those observations were obtained on four nights over a five-day period. To further examine these patterns, we display the residuals for each of the four nights in Figure 3, as a function of time. Clear trends are seen on each night, which are different for the primary and secondary components and have peak-to-peak excursions reaching 4 $\rm km\,s^{-1}$ in some cases, significantly larger than the velocity errors of 0.1–1.2 $\rm km\,s^{-1}$ (SR03). On some but not all nights, there appears to be a periodicity of roughly 0.20–0.25 days. The nature of these trends is unclear, particularly because this periodicity is much shorter than either the orbital or the rotational periods. Instrumental effects seem unlikely, but an explanation in terms of the considerable spottedness of both stars is certainly a distinct possibility. The Doppler imaging maps produced by SR03 show that both components display a very patchy distribution of surface features covering the polar regions. Individual features coming in and out of view as the stars rotate could easily be the cause of the systematic effects observed in the radial velocities, and the effects would not necessarily have to be the same on both stars, just as observed. Slight changes in the spots from one night to the next could account for the different patterns seen in Figure 3. The relatively large amplitude of the residual variations raises the concern that they may be affecting the velocity semi-amplitudes of the orbit, depending on the phase at which they occur. We do not see such trends in the CfA data, perhaps because our observations span a much longer time (more than 7 years, and $\sim$2200 rotational cycles), allowing for spots to change and average out these effects. We therefore proceed on the assumption that possible systematic effects of this nature on $K_{\rm p}$ and $K_{\rm s}$ are lessened in the CfA data.

5. The Visual Orbit Solution

The basic measured quantity from an interferometric observation is *visibility*, which evaluates the contrast in the fringe pattern obtained by combining starlight wave fronts from multiple apertures, filtered through a finite bandwidth. For a single star of angular diameter θ, the interferometric visibility V for a uniform disk model is given by,

$$V = \frac{2J_1(\pi B\theta/\lambda)}{\pi B\theta/\lambda}, \tag{1}$$

where J_1 is the first-order Bessel function, B is the projected baseline length as seen by the star, and λ is the observed bandpass central wavelength. The interferometric visibility for a binary, where the individual stars have visibilities $V_{\rm p}$ (primary) and $V_{\rm s}$ (secondary) per equation (1) above, is given by

$$V = \frac{\sqrt{(\beta^2 V_p^2 + V_s^2 + 2\beta V_p V_s \cos((2\pi/\lambda)\mathbf{B}\cdot\mathbf{s}))}}{1+\beta}, \tag{2}$$

where β is the primary to secondary flux ratio, $\mathbf{B}$ is the projected baseline vector as seen by the binary, and $\mathbf{s}$ is the binary's angular separation vector in the plane of the sky.

Using our measured interferometric visibilities and the above equations, we are able to augment the spectroscopic orbital solutions to derive a visual orbit for σ^2 CrB. Adopting the period and epoch of nodal passage from § 2.1, we now derive the parameters that can only be determined astrometrically: angular semimajor axis (α); inclination (i); and, longitude of the ascending node (Ω). We also treat the K'-band magnitude difference as a free parameter in order to test evolutionary models.

For a circular orbit, the epoch of periastron passage (T_0) is replaced by the epoch of ascending nodal passage ($T_{\rm node}$), defined as the epoch of fastest secondary recession, in the visual orbit equations (Heintz 1978). Accordingly, we translate the T value listed in § 2.1 by one-half of the orbital period to determine the epoch of the ascending nodal passage as $T_{\rm node} = 2{,}450{,}127.04855 \pm 0.00020$ (HJD) for use in our visual orbit solution. The 1-σ errors of this and other adopted parameters listed in Table 4 have been propagated to our error estimates for the derived parameters.

The angular diameters of the components are too small to be resolved by our K'-band observations. We therefore estimate these based on the components' absolute magnitudes and temperatures as described below. We first estimate the Johnson V-band magnitude of σ^2 CrB using its Tycho-2 magnitudes of $B_{\rm T} = 6.262 \pm 0.014$ and $V_{\rm T} = 5.620 \pm 0.009$ and the relation $V_{\rm J} = V_{\rm T} - 0.090(B_{\rm T} - V_{\rm T})$ from the Guide to the Tycho-2 Catalog. Then, using

the V-band flux ratio from § 2 and the Lestrade et al. (1999) parallax, we obtain absolute magnitudes of $M_{\rm V} = 4.35 \pm 0.02$ for the primary and $M_{\rm V} = 4.74 \pm 0.02$ for the secondary. These magnitudes lead to linear radius estimates of $1.2 R_{\odot}$ for the primary and $1.1 R_{\odot}$ for the secondary using the tabulation of stellar physical parameters in Popper (1980) and Andersen (1991). Finally, using the Lestrade et al. (1999) parallax, we adopt component angular diameters of $\theta_{\rm p} = 0.50$ mas and $\theta_{\rm s} = 0.45$ mas, propagating a 0.05 mas uncertainty in these values for deriving the uncertainty of our orbital elements. Diameter estimates using the temperatures of the components from § 2 are consistent with these values.

We conduct an exhaustive search of the parameter space for the unknown parameters mentioned, namely, α, i, Ω, and $\Delta K'$. The orbital inclination is constrained by the $a \sin i$ from spectroscopy, the free-parameter α, and the Lestrade et al. (1999) parallax. We impose this constraint during our exploration of the parameter space along with its associated 1-σ error. We explore the unknown parameters over many iterations, by randomly selecting them between broad limits and using equation (2) to evaluate the predicted binary visibility for the baseline and binary positions at each observational epoch. The orbital solution presented here represents the parameter set with the minimum χ^2 value when comparing the predicted and measured visibilities.

Figure 4 shows the measured visibilities (plus signs) with vertical error bars for each of the 26 observations, along with the computed model visibilities (diamonds), and Table 2 lists the corresponding numerical values of the observed and model visibilities along with the residuals of the fit. Table 4 summarizes the visual orbit parameters for σ^2 CrB from our solution and Figure 5 plots the visual orbit in the plane of the sky. As seen in Figure 5, we have a reasonably good phase coverage from our observations.

As mentioned in § 4.1, star spots can create systematic effects in the data obtained on this binary. These effects are especially significant for data obtained over a short time baseline, as seen for the SR03 spectroscopic solution. While our interferometric data span 73 days, allowing for some averaging of these effects, the bulk of the data used were obtained over 12 days, justifying an exploration of this effect. Specifically, the separation between the stars derived from our visibility data would represent the separation of the centers of light rather than that of mass. As discussed in Hummel et al. (1994), heavily-spotted stars will incur a systematic shift in the center of light from rotational and orbital motions, perhaps inducing an additional uncertainty in the orbital elements derived. We assume a spot-induced change in the angular semimajor axis of 2% of the primary's diameter, or 0.01 mas. This is less that the uncertainty of our derived semimajor axis, and at our baselines of 270–330 meters, translates to a 0.005–0.011 change in the visibility. While the uncertainties of our measured visibilities are an order of magnitude larger than this, we ran a test orbital fit by

adding a 0.010 uncertainty to the visibility errors as a root-sum-squared. While, as expected, the χ^2 of the fit improved, the values and uncertainties of the derived parameters remained unchanged, leading us to conclude that this effect, while real, is too small to affect our results.

We determine the 1, 2, and 3-σ uncertainties of each visual orbit parameter using a Monte Carlo simulation approach. We compute the orbital fit for 100,000 iterations, where for each iteration, we randomly select the adopted parameters within their respective 1-σ intervals and the model parameters around their corresponding best-fit solution, generating a multi-dimensional χ^2 "surface". Then, we project this surface along each parameter axis, resulting in the plots shown in Figures 6 to 9. The figures show the χ^2 distribution around the best-fit orbit and enable estimation of 1, 2, and 3-σ errors for each parameter based on a χ^2 deviation of 1, 4, and 9 units, respectively, from its minimum value. The horizontal dashed lines in the figures from bottom to top mark the minimum χ^2 value and those corresponding to 1, 2, and 3-σ errors, and Table 4 lists the corresponding numerical 1-σ errors of the model parameters.

6. Physical Parameters

6.1. Component Mass Estimates

Our angular semimajor axis obtained from interferometry translates to 0.0279 ± 0.0003 AU or 5.99 ± 0.07 $R_\odot$ using the Lestrade et al. (1999) parallax. Newton's generalization of Kepler's Third Law then yields a mass-sum of 2.227 ± 0.073 $M_\odot$ for the pair, and using the mass ratio from our spectroscopic solution of 0.9586 ± 0.0047, we get individual component masses of 1.137 ± 0.037 $M_\odot$ and 1.090 ± 0.036 $M_\odot$ for the primary and secondary, respectively. As noted in § 4.1, the SR03 velocities yield a significantly different mass ratio of 0.9746 ± 0.0016, but this 4-σ difference is not enough to influence the mass estimates significantly. The uncertainty in our masses is dominated by the cubed semimajor axis factor in estimating the mass sum, resulting in about a 3% uncertainty in mass-sum corresponding to a 1% uncertainty in the semimajor axis. The high precision of the mass ratio from the spectroscopic solution results in final masses of 3% uncertainty as well. Component mass estimates using the SR03 velocities are 1.128 ± 0.037 and 1.099 ± 0.036, in excellent agreement with the masses using our velocities. These masses along with other physical parameters derived are listed in Table 5.

6.2. Radii of the Components

Assuming synchronous and co-aligned rotation of spherical components, reasonable given the short orbital period and evidence from SR03 of unevolved stars contained within their Roche limits, we can estimate the component radii from the measured spectroscopic $v \sin i$. As mentioned in § 2, our spectra yield $v \sin i = 26 \pm 1$ km s^{-1} for both the primary and secondary. These values and uncertainties are identical to those in SR03. Using the inclination from our visual orbit, and adopting the orbital period from spectroscopy as the rotational period, we get identical component radii of 1.244 ± 0.050 $R_\odot$ for the primary and secondary. This translates to an angular diameter of 0.509 ± 0.020 mas for each component using the Lestrade et al. (1999) parallax, in excellent agreement with our adopted diameter for the primary and a 1-σ variance for the secondary, given our associated 0.05-mas errors for these values. These radii estimates, along with the effective temperatures from § 2 and the relation $L \propto R^2 T_{\rm eff}^4$, lead to a luminosity ratio of 0.89 ± 0.16. Alternatively, using bolometric corrections from Flower (1996) of $BC_{\rm p} = -0.038 \pm 0.017$ and $BC_{\rm s} = -0.064 \pm 0.020$ corresponding to the components' effective temperatures, the V-band flux ratio of 0.70 ± 0.02 from spectroscopy translates to a total luminosity ratio of 0.68 ± 0.20, a 1-σ variance from the estimate above. Conversely, our estimates of effective temperature and luminosity ratio require a radius ratio of 0.88 ± 0.14, again at a 1-σ variance from the 1.00 ± 0.06 estimate from the identical $v \sin i$ values of the components.

6.3. Absolute Magnitudes and Ages

We allowed the K'-band magnitude difference to be a free parameter for our visual orbit fit, obtaining $\Delta K' = 0.19 \pm 0.19$, consistent with the 0.18 estimate from the mass-luminosity relations of Henry & McCarthy (1993)[6]. The uncertainty in $\Delta K'$ is large because visibility measurements of nearly equal mass, and hence nearly equal brightness, pairs are relatively insensitive to the magnitude difference of the components (Hummel et al. 1998; Boden et al. 1999). Using equation (2), we have verified that a 10% change in $\Delta K'$ for σ^2 CrB results in only 0.1% change in visibility. This, along with the poor quality K magnitude listed in 2MASS (for σ^2 CrB, $K = 4.052 \pm 0.036$, but flagged as a very poor fit), thwart any attempts to use these magnitudes for checking stellar evolution models. However, we can revert to V-band photometry to explore this topic.

[6]The relations from Henry & McCarthy are for 0.5 $M_\odot \leq$ Mass $\leq$ 1.0 $M_\odot$. We consider it safe to extrapolate out to our estimated masses of slightly larger than 1.0 $M_\odot$.

In § 5, we derived the absolute V-band magnitudes of the components of σ^2 CrB as $M_{\rm V} = 4.35 \pm 0.02$ for the primary and $M_{\rm V} = 4.74 \pm 0.02$ for the secondary. For σ^1 CrB, we similarly use the Tycho-2 magnitudes and the Lestrade et al. (1999) parallax to obtain $M_{\rm V} = 4.64 \pm 0.01$. SR03 had a smaller magnitude difference for the components of σ^2 CrB, and the corresponding results using their spectroscopy are also included in Table 5 along with the values from their paper. Figure 10 plots these three stars on an H-R diagram using our magnitude and temperature estimates, along with isochrones for 0.5, 1.5, 3.0, and 5.0 Gyr ages (left to right) from the Yonsei-Yale isochrones (dotted, Yi et al. 2001) and the Victoria-Regina stellar evolution models (dashed, VandenBerg et al. 2006) for solar metallicity (see Footnote 3).

Wright et al. (2004) estimate an age of 1.8 Gyr for σ^1 CrB based on chromospheric activity, and Valenti & Fischer (2005) estimate an age of 5.0 Gyr from spectroscopy with limits of 2.9–7.8 Gyr based on 1-σ changes to log$L$. SR03 identify a much lower age, of a few times 10^7 years, by matching pre-main-sequence evolutionary tracks and point to their higher Li abundance as supporting evidence. While abundance determinations in double-lined spectroscopic binaries are particularly difficult and more prone to errors, the high Li abundance of 2.60 ± 0.03 (SR03) for the slow-rotating single-lined companion σ^1 CrB does argue for a young system. Each point along the isochrones plotted in Figure 10 corresponds to a particular mass, allowing us to use our mass estimates for the components of σ^2 CrB to further constrain the system's age. Our mass, luminosity, and temperature estimates indicate an age for this system of 0.5–1.5 Gyr, with a range of 0.1–3 Gyr permissible within 1-σ errors.

6.4. Mass Estimate of σ^1 CrB

Our mass estimates for the components of σ^2 CrB allow us to constrain the mass of the wider visual companion σ^1 CrB as well. Scardia (1979) presented an improved visual orbit for the AB pair based on 886 observations spanning almost 200 years of observation, yielding $P = 889$ years, $a = 5\farcs9$, $i = 31\fdg8$, $e = 0.76$, and $\Omega = 16\fdg9$. However, he did not publish uncertainties for these parameters, and given the long period, his less than one-third phase coverage leads to only a preliminary orbital solution, albeit one that convincingly shows orbital motion of the pair. He further uses parallaxes available to him to derive a mass-sum for the AB system of 3.2 $M_\odot$. We used all current WDS observations, adding almost 200 observations since Scardia (1979), to update this orbit and obtain uncertainties for the parameters. Our visual orbit is presented in Figure 11, along with the Scardia orbit for comparison, and Table 6 lists the derived orbital elements. Adopting the Lestrade et al.

(1999) parallax of the A component, we estimate a mass-sum of $3.2 \pm 0.9\ M_{\odot}$, resulting in a B-component mass estimate of $1.0\ M_{\odot}$, consistent with its spectral type of G1 V (Gray et al. 2003). Valenti & Fischer (2005) estimate a mass of $0.77 \pm 0.21\ M_{\odot}$ based on high-resolution spectroscopy, but we believe that they systematically underestimate their uncertainty by overlooking the $\log e$ factor in converting from uncertainty in $\log L$ to uncertainty in L. Using the $\log e$ factor, we followed their methods to obtain a mass estimate of $0.77 \pm 0.44\ M_{\odot}$. The mass-error is dominated by the uncertainty of the Gliese & Jahreiß (1991) parallax used by Valenti & Fischer (2005). Adopting the higher precision Lestrade et al. (1999) parallax of the primary, we follow their method, and using the $\log e$ factor, get a mass estimate of $0.78 \pm 0.11\ M_{\odot}$. This mass is too low for the spectral type (as well as our own estimate of the effective temperature; see § 2) and the expectation from the visual orbit. A possible contamination of the secondary's spectral type from the $7''$ distant primary is unlikely, as determined by Richard Gray at our request from new spectroscopic observations (R. Gray 2008, private communication).

The inclination and longitude of the ascending node for this visual orbit are similar to those of the inner (σ^2 CrB) orbit, suggesting coplanarity. For the outer visual orbit, we can use our radial velocity estimate for σ^1 CrB, our derived systemic velocity for σ^2 CrB, and the speckle observations to unambiguously determine the longitude of the ascending node as $\Omega = 28\overset{\circ}{.}0 \pm 0\overset{\circ}{.}5$. Using the equation for the relative inclination of the two orbits (ϕ) from Fekel (1981), we get $\phi = 4\overset{\circ}{.}7$ or $60\overset{\circ}{.}3$, given the 180° ambiguity in Ω for the inner orbit, confirming coplanarity as a possibility.

7. The Wide Components: Optical or Physical?

In addition to the three solar-type stars, the WDS lists three additional components for σ CrB. We present evidence to show that WDS components C and D are optical alignments, while component E, itself a binary, is a physical association. WDS component C (ADS 9979C), measured $18''$ away at 103° in 1984 (Popović 1986) has a proper motion of $\mu_{\alpha} = -0\overset{''}{.}016\ \mathrm{yr}^{-1}$ and $\mu_{\delta} = -0\overset{''}{.}015\ \mathrm{yr}^{-1}$ (Jeffers et al. 1963), significantly different from that of σ^2 CrB of $\mu_{\alpha} = -0\overset{''}{.}26364 \pm 0\overset{''}{.}00091\ \mathrm{yr}^{-1}$ and $\mu_{\delta} = -0\overset{''}{.}09259 \pm 0\overset{''}{.}00129\ \mathrm{yr}^{-1}$ from van Leeuwen (2007). Similarly, component D, measured $88''$ away at 82° in 1996 (Courtot 1996) and clearly seen by us as a field star by blinking the multi-epoch STScI Digitized Sky Survey[7] (DSS) images, has a proper motion of $\mu_{\alpha} = +0\overset{''}{.}004\ \mathrm{yr}^{-1}$ and $\mu_{\delta} = -0\overset{''}{.}017\ \mathrm{yr}^{-1}$ (Jeffers et al. 1963), again significantly different from that of σ^2 CrB. As a confirmation of the

[7] `http://stdatu.stsci.edu/cgi-bin/dss_form`

optical alignment, we compare in Figures 12 and 13 the observed separations of components C and D, respectively, from the primary with the corresponding expected values based on their proper motions. The solid line is a linear fit to the published measurements from the WDS and the dashed line is the expected separation based on differential proper motion. The excellent agreement between the two lines for both components confirms them as field stars.

WDS component E (σ CrB C, HIP 79551) is widely separated from the primary at 635″, translating to a minimum physical separation of over 14,000 AU using the Lestrade et al. (1999) parallax. Despite its wide separation, this component appears to be physically associated with σ CrB based on its matching parallax of $\pi = 45.40 \pm 3.71$ mas and proper motion of $\mu_\alpha = -0\farcs26592 \pm 0\farcs00299$ yr^{-1} and $\mu_\delta = -0\farcs08363 \pm 0\farcs00368$ yr^{-1} (van Leeuwen 2007). While seemingly extreme for gravitationally bound systems, physical association has been demonstrated for pairs with separations out to 20,000 AU (e.g., Latham et al. 1991; Poveda et al. 1994). σ CrB C has a spectral classification of M2.5V (Reid et al. 1995), apparent magnitude of $V = 12.24$ (Bidelman 1985), and has itself been identified as a photocentric-motion binary with an unseen companion of 0.1 $M_\odot$ in a 52-year orbit (Heintz 1990). Perryman & ESA (1997) also identifies this star as a binary of type 'X' or stochastic solution, implying a photocenter wobble for an unresolved star, but for which the *Hipparcos* data are not sufficient to derive an orbit.

8. Conclusion

Augmenting our radial velocity measurements with published values, we obtain a coverage of nearly 86 years or 27,500 orbital cycles, resulting in a very precise ephemeris of $P = 1.139791423 \pm 0.000000080$ days and $T = 2{,}450{,}127.61845 \pm 0.00020$ (HJD) and a robust spectroscopic orbit for σ^2 CrB. Using the CHARA Array, we have resolved this 1.14-day spectroscopic binary, the shortest period system yet resolved, and derived its visual orbit. The resulting component masses are 1.137 ± 0.037 $M_\odot$ and 1.090 ± 0.036 $M_\odot$ for the primary and secondary, respectively. Our spectroscopy supports prior efforts in estimating the same $v \sin i$ values for both components, which assuming a synchronized, co-aligned rotation, results in equal radii of 1.244 ± 0.050 $R_\odot$ for both components. The corresponding radius ratio is consistent within 1-σ with its estimate using the components' temperatures and flux ratio from spectroscopy. We have also shown that this binary resides in a hierarchical quintuple system, composed of three close Sun-like stars and a wide M-dwarf binary. The wider visual orbit companion, σ^1 CrB, is about 7″ away in a 726-year visual orbit with $i = 32\fdg3$, which appears to be coplanar with the inner orbit. A comparison of the mass and absolute magni-

tude estimates of σ^1 CrB and σ^2 CrB with current stellar evolution models indicates a young age for the system of 1–3 Gyr, consistent with the relatively high Li abundance previously measured. Finally, the widest member of this system is an M-dwarf binary, σ CrB C, at a minimum separation of 14,000 AU. Figure 14 depicts the system's hierarchy in a pictorial form.

We thank Andy Boden and Doug Gies for their many useful suggestions that improved the quality of this work, and Richard Gray for making new observations at our request to confirm the spectral typing of the components. The CfA spectroscopic observations of σ^1 CrB and σ^2 CrB used in this paper were obtained with the help of J. Caruso, R. P. Stefanik, and J. Zajac. We also thank the CHARA Array operator P. J. Goldfinger for obtaining some of the data used here and for her able assistance of remote operations of the Array from AROC. Research at the CHARA Array is supported by the College of Arts and Sciences at Georgia State University and by the National Science Foundation through NSF grant AST-0606958. GT acknowledges partial support for this work from NSF grant AST-0708229 and NASA's MASSIF SIM Key Project (BLF57-04). This research has made use of the SIMBAD literature database, operated at CDS, Strasbourg, France, and of NASA's Astrophysics Data System. This effort used multi-epoch images from the Digitized Sky Survey, which was produced at the Space Telescope Science Institute under U.S. Government grant NAG W-2166. This publication also made use of data products from the Two Micron All Sky Survey (2MASS), which is a joint project of the University of Massachusetts and the Infrared Processing and Analysis Center/California Institute of Technology, funded by the National Aeronautics and Space Administration and the National Science Foundation.

REFERENCES

Andersen, J. 1991, A&A Rev., 3, 91

Baines, E. K., van Belle, G. T., ten Brummelaar, T. A., McAlister, H. A., Swain, M., Turner, N. H., Sturmann, L., & Sturmann, J. 2007, ApJ, 661, L195

Bakos, G. A. 1984, AJ, 89, 1740

Bidelman, W. P. 1985, ApJS, 59, 197

Boden, A. F., et al. 1999, ApJ, 527, 360

Cohen, M., Wheaton, W. A., & Megeath, S. T. 2003, AJ, 126, 1090

Colina, L., Bohlin, R. C., & Castelli, F. 1996, AJ, 112, 307

Courtot, J.-F. 1996, Observations et Travaux, 47, 47

Duquennoy, A., & Mayor, M. 1991, A&A, 248, 485

Fallon, T., McAlister, H. A., & ten Brummelaar, T. A. 2003, Proc. SPIE, 4838, 1193

Fekel, F. C., Jr. 1981, ApJ, 246, 879

Flower, P. J. 1996, ApJ, 469, 355

Fuhrmann, K. 2004, AN, 325, 3

Gliese, W., & Jahreiß, H. 1991, On: The Astronomical Data Center CD-ROM: Selected Astronomical Catalogs, Vol. I; L.E. Brotzmann, S.E. Gesser (eds.), NASA/Astronomical Data Center, Goddard Space Flight Center, Greenbelt, MD

Gray, R. O., Corbally, C. J., Garrison, R. F., McFadden, M. T., & Robinson, P. E. 2003, AJ, 126, 2048

Grenier, S., Gomez, A. E., Jaschek, C., Jaschek, M., & Heck, A. 1985, A&A, 145, 331

Harper, W. E. 1925, Publications of the Dominion Astrophysical Observatory Victoria, 3, 225

Heintz, W. D. 1978, Double Stars (Reidel: Dordrecht), p.32

Heintz, W. D. 1990, AJ, 99, 420

Henry, T. J., & McCarthy, D. W., Jr. 1993, AJ, 106, 773

Hummel, C. A., Armstrong, J. T., Quirrenbach, A., Buscher, D. F., Mozurkewich, D., Simon, R. S., & Johnston, K. J. 1993, AJ, 106, 2486

Hummel, C. A., Armstrong, J. T., Quirrenbach, A., Buscher, D. F., Mozurkewich, D., Elias, N. M., II, & Wilson, R. E. 1994, AJ, 107, 1859

Hummel, C. A., Mozurkewich, D., Armstrong, J. T., Hajian, A. R., Elias, N. M., II, & Hutter, D. J. 1998, AJ, 116, 2536

Jeffers, H. M., van den Bos, W. H., & Greeby, F. M. 1963, Publications of the Lick Observatory, Mount Hamilton: University of California, Lick Observatory

Latham, D. W., Davis, R. J., Stefanik, R. P., Mazeh, T., & Abt, H. A. 1991, AJ, 101, 625

Latham, D. W. 1992, in IAU Coll. 135, Complementary Approaches to Double and Multiple Star Research, ASP Conf. Ser. 32, eds. H. A. McAlister & W. I. Hartkopf (San Francisco: ASP), 110

Latham, D. W., Nordström, B., Andersen, J., Torres, G., Stefanik, R. P., Thaller, M., & Bester, M. 1996, A&A, 314, 864

Latham, D. W., Stefanik, R. P., Torres, G., Davis, R. J., Mazeh, T., Carney, B. W., Laird, J. B., & Morse, J. A. 2002, AJ, 124, 1144

Lestrade, J.-F., Preston, R. A., Jones, D. L., Phillips, R. B., Rogers, A. E. E., Titus, M. A., Rioja, M. J., & Gabuzda, D. C. 1999, A&A, 344, 1014

McAlister, H. A., et al. 2005, ApJ, 628, 439

Monnier, J. D., et al. 2007, Science, 317, 342

Nordström, B., Latham, D. W., Morse, J. A., Milone, A. A. E., Kurucz, R. L., Andersen, J., & Stefanik, R. P. 1994, A&A, 287, 338

Nordström, B., Mayor, M., Andersen, J., Holmberg, J., Pont, F., Jørgensen, B. R., Olsen, E. H., Udry, S., & Mowlavi, N. 2004, A&A, 418, 989

Perryman, M. A. C., & ESA 1997, ESA Special Publication, 1200 (Noordwijk: ESA)

Popović, G. M. 1986, Bulletin de l'Observatoire Astronomique de Belgrade, 136, 84

Popper, D. M. 1980, ARA&A, 18, 115

Poveda, A., Herrera, M. A., Allen, C., Cordero, G., & Lavalley, C. 1994, Revista Mexicana de Astronomia y Astrofisica, 28, 43

Reid, I. N., Hawley, S. L., & Gizis, J. E. 1995, AJ, 110, 1838

Scardia, M. 1979, Astronomische Nachrichten, 300, 307

Strassmeier, K. G., & Rice, J. B. 2003, A&A, 399, 315, (SR03)

ten Brummelaar, T. A., et al. 2005, ApJ, 628, 453

Torres, G., Stefanik, R. P., Andersen, J., Nordström, B., Latham, D. W., & Clausen, J. V. 1997, AJ, 114, 2764

Valenti, J. A., & Fischer, D. A. 2005, ApJS, 159, 141

VandenBerg, D. A., Bergbusch, P. A., & Dowler, P. D. 2006, ApJS, 162, 375

van Leeuwen, F. 2007, Hipparcos, the New Reduction of the Raw Data (Springer Dordrecht)

Wright, J. T., Marcy, G. W., Butler, R. P., & Vogt, S. S. 2004, ApJS, 152, 261

Yi, S., Demarque, P., Kim, Y.-C., Lee, Y.-W., Ree, C. H., Lejeune, T., & Barnes, S. 2001, ApJS, 136, 417

Zucker, S., & Mazeh, T. 1994, ApJ, 420, 806

Table 1. Radial Velocities of σ^2 CrB

HJD (2,400,000+)	$RV_{\rm p}$ ($\rm km\,s^{-1}$)	$RV_{\rm s}$ ($\rm km\,s^{-1}$)	$\sigma_{RV_{\rm p}}$ ($\rm km\,s^{-1}$)	$\sigma_{RV_{\rm s}}$ ($\rm km\,s^{-1}$)	$(O-C)_{\rm p}$ ($\rm km\,s^{-1}$)	$(O-C)_{\rm s}$ ($\rm km\,s^{-1}$)	Orbital Phase
48764.6474	6.88	−36.45	2.68	2.84	−1.72	−0.87	0.193
48781.6495	35.46	−64.08	2.99	3.16	1.15	−1.68	0.109
48810.6618	−69.00	46.22	1.16	1.23	0.47	0.37	0.564
48813.6236	18.25	−46.52	1.19	1.26	−0.89	0.06	0.162
48820.6185	−31.35	5.07	1.61	1.71	0.24	−1.27	0.299
48822.6494	41.46	−69.41	1.32	1.40	0.97	−0.55	0.081
48826.5581	−74.53	52.87	1.19	1.26	−0.38	2.13	0.510
48828.6849	−56.96	31.25	1.37	1.45	−0.33	−1.21	0.376
48838.5942	43.01	−71.62	1.15	1.22	0.62	−0.79	0.070
50258.6759	48.63	−75.42	1.43	1.51	0.73	1.17	0.984
50260.6371	−31.00	4.33	0.85	0.90	−0.66	−0.71	0.704
50263.6316	−42.68	17.76	0.83	0.88	0.40	−0.56	0.332
50266.6225	46.61	−73.03	0.99	1.04	0.74	1.43	0.956
50269.7633	−27.25	2.84	0.99	1.05	0.53	0.47	0.711
50271.6269	−46.41	23.01	0.95	1.01	1.46	−0.31	0.346
50275.6464	29.47	−57.26	0.97	1.03	−0.22	0.33	0.873
50285.6440	−49.95	26.91	0.90	0.95	0.84	0.54	0.644
50287.6352	−60.98	37.03	0.89	0.94	−0.45	0.51	0.391
50292.5697	−23.39	−1.49	1.02	1.08	0.90	−0.22	0.721
50295.6335	−65.17	39.49	0.79	0.83	−0.72	−1.13	0.409
50298.5502	46.99	−75.36	0.71	0.75	0.03	0.24	0.968
50300.5553	−22.15	−4.43	0.80	0.85	−0.21	−0.70	0.727
50302.6499	−69.55	44.72	0.84	0.89	−0.23	−0.98	0.565
50346.5051	46.86	−76.63	0.92	0.97	0.65	−1.81	0.041
50348.5107	4.35	−29.89	0.99	1.04	−1.77	3.10	0.801
50350.5649	−63.76	38.37	0.81	0.86	−1.83	0.39	0.603
50352.4779	−24.23	−1.41	0.79	0.84	0.74	−0.84	0.281
50356.4742	−0.04	−26.85	0.79	0.84	−1.27	1.05	0.787
50358.4740	−72.84	50.15	0.77	0.81	−0.68	1.49	0.542
50361.4826	13.31	−40.12	0.80	0.85	0.79	−0.45	0.182
50364.4624	1.84	−29.15	0.86	0.91	−2.54	2.04	0.796
50374.4574	−70.50	44.94	0.85	0.90	−1.26	−0.67	0.565
50379.4665	45.29	−73.75	0.82	0.87	−0.99	1.14	0.960
50383.4500	−70.47	48.43	0.84	0.89	1.34	0.13	0.455
50385.4760	−6.74	−19.80	0.81	0.86	−0.54	0.35	0.232
50388.4407	15.96	−44.52	0.92	0.97	−1.63	0.45	0.833

Table 1—Continued

HJD (2,400,000+)	$RV_{\rm p}$ ($\rm km\,s^{-1}$)	$RV_{\rm s}$ ($\rm km\,s^{-1}$)	$\sigma_{RV_{\rm p}}$ ($\rm km\,s^{-1}$)	$\sigma_{RV_{\rm s}}$ ($\rm km\,s^{-1}$)	$(O-C)_{\rm p}$ ($\rm km\,s^{-1}$)	$(O-C)_{\rm s}$ ($\rm km\,s^{-1}$)	Orbital Phase
50391.4280	−71.44	49.52	0.81	0.86	0.32	1.28	0.454
50590.7488	−41.53	17.65	0.98	1.04	0.68	0.24	0.329
50619.6791	−26.78	3.14	1.05	1.11	1.06	0.72	0.711
50846.9255	39.45	−68.48	0.90	0.95	0.06	−0.78	0.087
51216.9001	−35.81	12.55	1.98	2.09	1.52	0.23	0.685
51246.7808	36.69	−66.52	2.01	2.13	−0.06	−1.57	0.901
51279.6859	−5.90	−19.52	2.51	2.65	−0.71	1.68	0.770
51341.7199	6.97	−33.48	1.77	1.87	−0.33	0.75	0.196
51374.6086	44.93	−73.34	2.01	2.12	−0.16	0.31	0.051
51374.6112	45.14	−74.26	3.08	3.26	0.34	−0.91	0.054

Table 2. Interferometric Visibilities for σ^2 CrB

HJD (2,400,000+)	Measured V	σ_V	Model V	$(O-C)_V$	u (m)	v (m)	Hour Angle (h)
54237.763	0.864	0.086	0.783	0.081	202.4	250.7	−2.24
54237.774	0.909	0.107	0.775	0.134	196.7	258.2	−1.99
54237.784	0.736	0.062	0.759	−0.022	190.3	265.2	−1.74
54237.796	0.702	0.063	0.729	−0.027	182.4	272.6	−1.46
54237.806	0.585	0.058	0.688	−0.103	174.6	278.9	−1.22
54237.816	0.652	0.076	0.625	0.027	165.6	285.3	−0.97
54237.833	0.468	0.053	0.474	−0.006	149.7	294.7	−0.56
54237.932	0.833	0.049	0.833	0.001	30.4	326.9	1.82
54237.942	0.775	0.059	0.791	−0.017	17.1	327.7	2.05
54237.954	0.672	0.038	0.672	0.001	0.5	328.1	2.34
54237.980	0.244	0.015	0.247	−0.004	−35.3	326.5	2.98
54247.701	0.858	0.113	0.887	−0.029	159.9	214.9	−3.08
54247.716	0.888	0.080	0.863	0.025	154.1	223.0	−2.73
54247.729	0.824	0.083	0.785	0.040	147.5	230.2	−2.40
54247.744	0.669	0.093	0.644	0.025	139.1	237.6	−2.05
54247.761	0.435	0.058	0.430	0.005	128.1	245.6	−1.64
54249.714	0.589	0.053	0.621	−0.032	152.1	225.3	−2.63
54249.726	0.570	0.054	0.609	−0.039	146.6	231.1	−2.36
54249.739	0.575	0.064	0.573	0.002	138.6	238.1	−2.03
54249.751	0.594	0.063	0.524	0.070	131.3	243.5	−1.75
54249.772	0.391	0.059	0.376	0.015	115.7	252.8	−1.24
54310.716	0.616	0.062	0.526	0.090	48.7	325.0	1.49
54310.726	0.405	0.050	0.410	−0.005	35.8	326.4	1.72
54310.776	0.477	0.050	0.454	0.023	−31.5	326.8	2.91
54310.786	0.558	0.054	0.619	−0.061	−45.5	325.4	3.16
54310.797	0.870	0.100	0.745	0.125	−59.5	323.5	3.42

Table 3. Spectroscopic Orbital Solutions for σ^2 CrB

Element	This Work	SR03 Velocities[a]	SR03 Results
Orbital Elements:			
P (days)	$1.139791423 \pm 0.000000080$[b]	$1.139791423 \pm 0.000000080$[b]	1.1397912 (adopted)
T (HJD-2,400,000)[c]	$50{,}127.61845 \pm 0.00020$[b]	$50{,}127.61845 \pm 0.00020$[b]	50,127.6248[d]
e	0.0[e]	0.0[e]	0.0[e]
ω (deg)	0.0[e]	0.0[e]	0.0[e]
γ (km s^{-1})	-13.03 ± 0.11	-12.58 ± 0.05	-12.3 ± 0.06
$K_{\rm p}$ (km s^{-1})	61.25 ± 0.21	61.31 ± 0.06	61.34 ± 0.06
$K_{\rm s}$ (km s^{-1})	63.89 ± 0.22	62.90 ± 0.08	62.91 ± 0.08
Derived quantities:			
$M_{\rm p} \sin^3 i$ ($M_\odot$)	0.11818 ± 0.00092	0.11461 ± 0.00032	0.1147
$M_{\rm s} \sin^3 i$ ($M_\odot$)	0.11329 ± 0.00086	0.11170 ± 0.00027	0.1118
$q \equiv M_{\rm s}/M_{\rm p}$	0.9586 ± 0.0047	0.9746 ± 0.0016	0.975 ± 0.002
$a_{\rm p} \sin i$ (10^6 km)	0.9600 ± 0.0033	0.96085 ± 0.00097	0.96138 ± 0.00093
$a_{\rm s} \sin i$ (10^6 km)	1.0014 ± 0.0035	0.98592 ± 0.00126	0.9861 ± 0.0012
$a \sin i$ ($R_\odot$)	2.8181 ± 0.0068	2.7971 ± 0.0023	2.798 ± 0.002
Other quantities pertaining to the fit:			
$N_{\rm obs}$	46	217	217
Time span (days)	2610	5.4	5.4
$\sigma_{\rm p}$ (km s^{-1})[f]	1.04	0.74	0.71
$\sigma_{\rm s}$ (km s^{-1})[f]	1.10	0.97	...

[a]Our orbital solution using SR03 velocities.

[b]Determined using all published velocities (see § 2.1)

[c]T is the epoch of maximum primary velocity.

[d]The value from SR03 has been shifted by an integer number of cycles to the epoch derived in this work,

for comparison purposes.

[e]Circular orbit adopted.

[f]RMS residual from the fit.

Table 4. Visual Orbit Solution for σ^2 CrB

Orbital Parameter	Value
Adopted values:	
Period (days)	$1.139791423 \pm 0.000000080$[a]
$T_{\rm node}$ (HJD-2,400,000)[b]	$50{,}127.04855 \pm 0.00020$
e	0.0[c]
ω (deg)	0.0[c]
$\theta_{\rm p}$ (mas)	0.50 ± 0.05[d]
$\theta_{\rm s}$ (mas)	0.45 ± 0.05[d]
Visual orbit parameters:	
α (mas)	1.225 ± 0.013
i (deg)	28.08 ± 0.34
Ω (deg)	207.93 ± 0.67[e]
$\Delta K'$	0.19 ± 0.19
Reduced χ^2	0.61[f]

[a]See § 2.1.

[b]This is the epoch of the ascending node, defined as the epoch of maximum secondary velocity, and accordingly is one-half period less than the value in Table 3 (see § 5).

[c]Circular orbit adopted.

[d]See § 5.

[e]This value suffers from a 180° ambiguity due to the cosine term in Equation (2).

[f]The low χ^2 indicates that our error estimates for visibility are conservative.

Table 5. Physical parameters for σ^2 CrB

	This Work		SR03 Spectroscopy[a]		SR03 Results	
Physical Parameter	Primary	Secondary	Primary	Secondary	Primary	Secondary
a ($R_\odot$)	5.99 ± 0.07		5.99 ± 0.07		...	
Mass ($M_\odot$)	1.137 ± 0.037	1.090 ± 0.036	1.128 ± 0.037	1.099 ± 0.036	1.108 ± 0.004[b]	1.080 ± 0.004[b]
Radius ($R_\odot$)	1.244 ± 0.050	1.244 ± 0.050	1.244 ± 0.050	1.244 ± 0.050	1.14 ± 0.04	1.14 ± 0.04
$T_{\rm eff}$ (K)	6050 ± 150	5870 ± 150	6000 ± 50	5900 ± 50	6000 ± 50	5900 ± 50
$M_{\rm V}$ (mag)	4.35 ± 0.02	4.74 ± 0.02	4.45 ± 0.02	4.61 ± 0.02	4.61 ± 0.07	4.76 ± 0.07
$M_{\rm K}$ (mag)	2.93 ± 0.09	3.12 ± 0.11	...	...	...	...

[a]These parameters use the SR03 spectroscopic results such as flux ratio, rotational velocities, and radial velocities, but use the Lestrade et al. (1999) parallax, Tycho-2 magnitudes, and our visual orbit.

[b]As noted in § 1, these uncertainties are unrealistically small.

Table 6. Visual Orbit Solution for $\sigma^1 - \sigma^2$ CrB

Orbital Parameter	Value
P (years)	726 ± 62
T_0 (BY)	1,825.2 ± 1.5
e	0.72 ± 0.01
ω (deg)	237.3 ± 6.8
α (arcsec)	5.26 ± 0.35
i (deg)	32.3 ± 4.1
Ω (deg)	28.0 ± 0.5

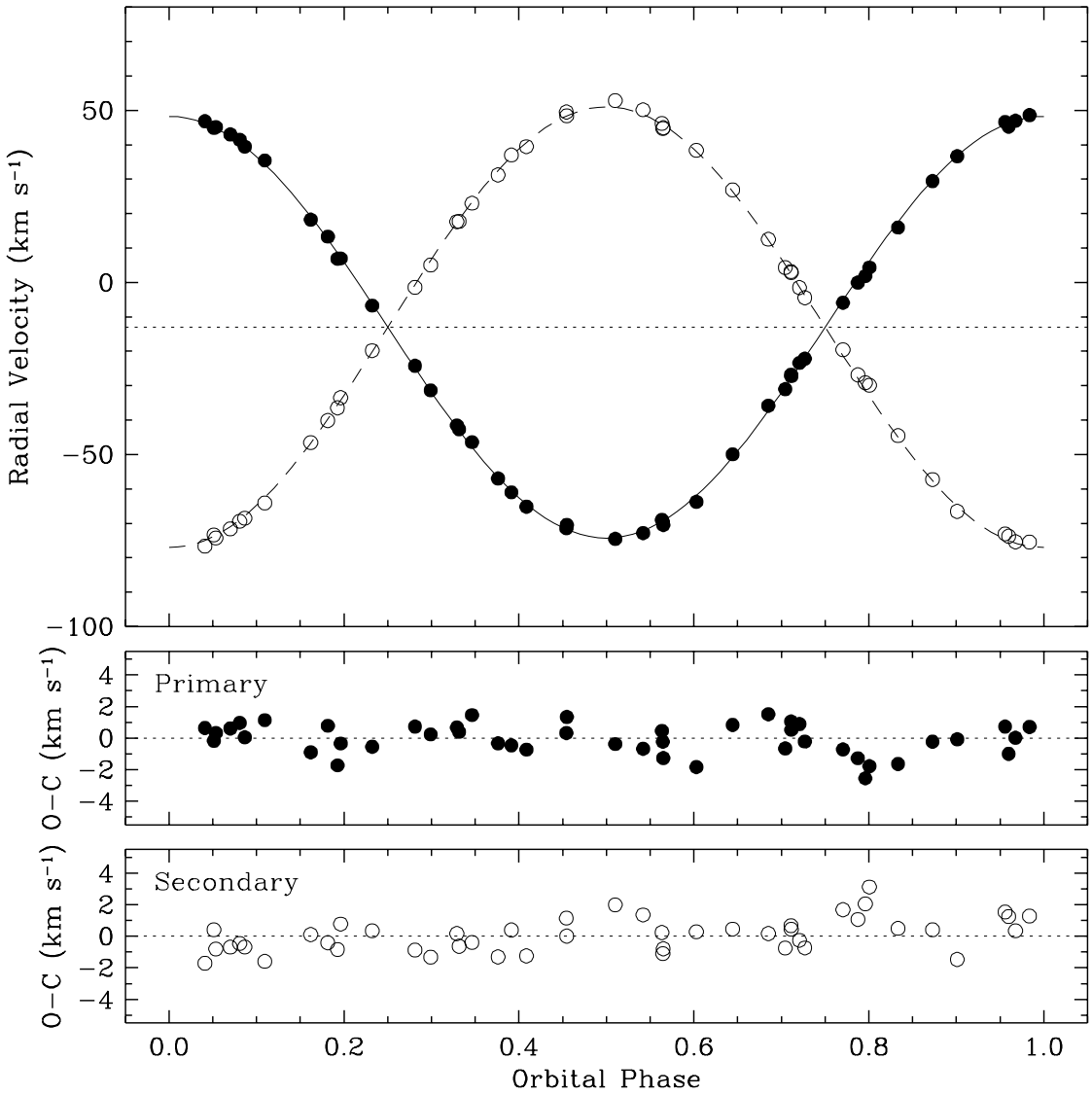

Fig. 1.— Our radial velocities and the orbital fit for σ^2 CrB (top panel) and the primary and secondary residuals (bottom panels). Filled circles represent the primary and open circles represent the secondary component. The corresponding orbital elements are listed in Table 3.

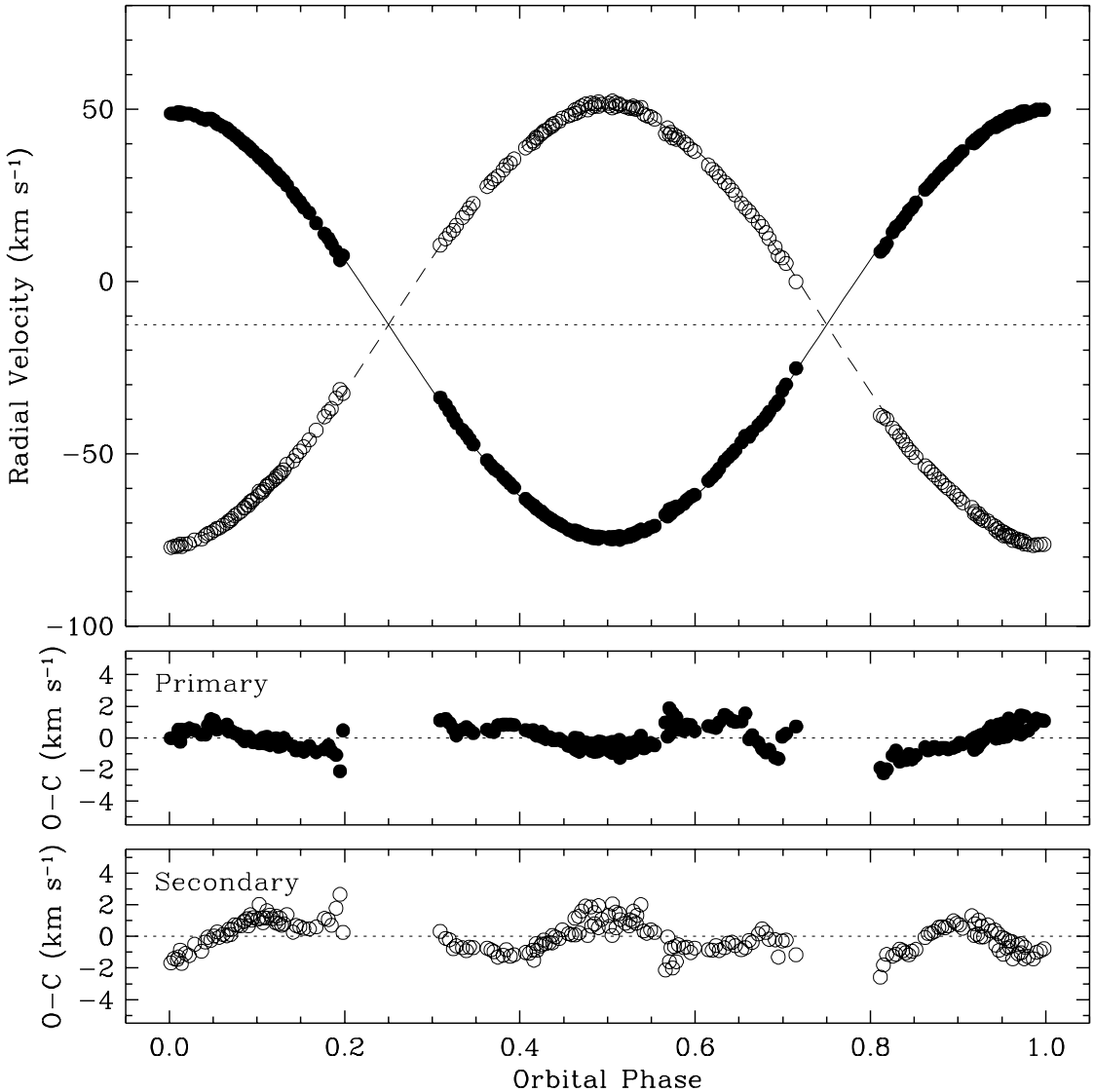

Fig. 2.— Same as Figure 1 but based on SR03 radial velocities.

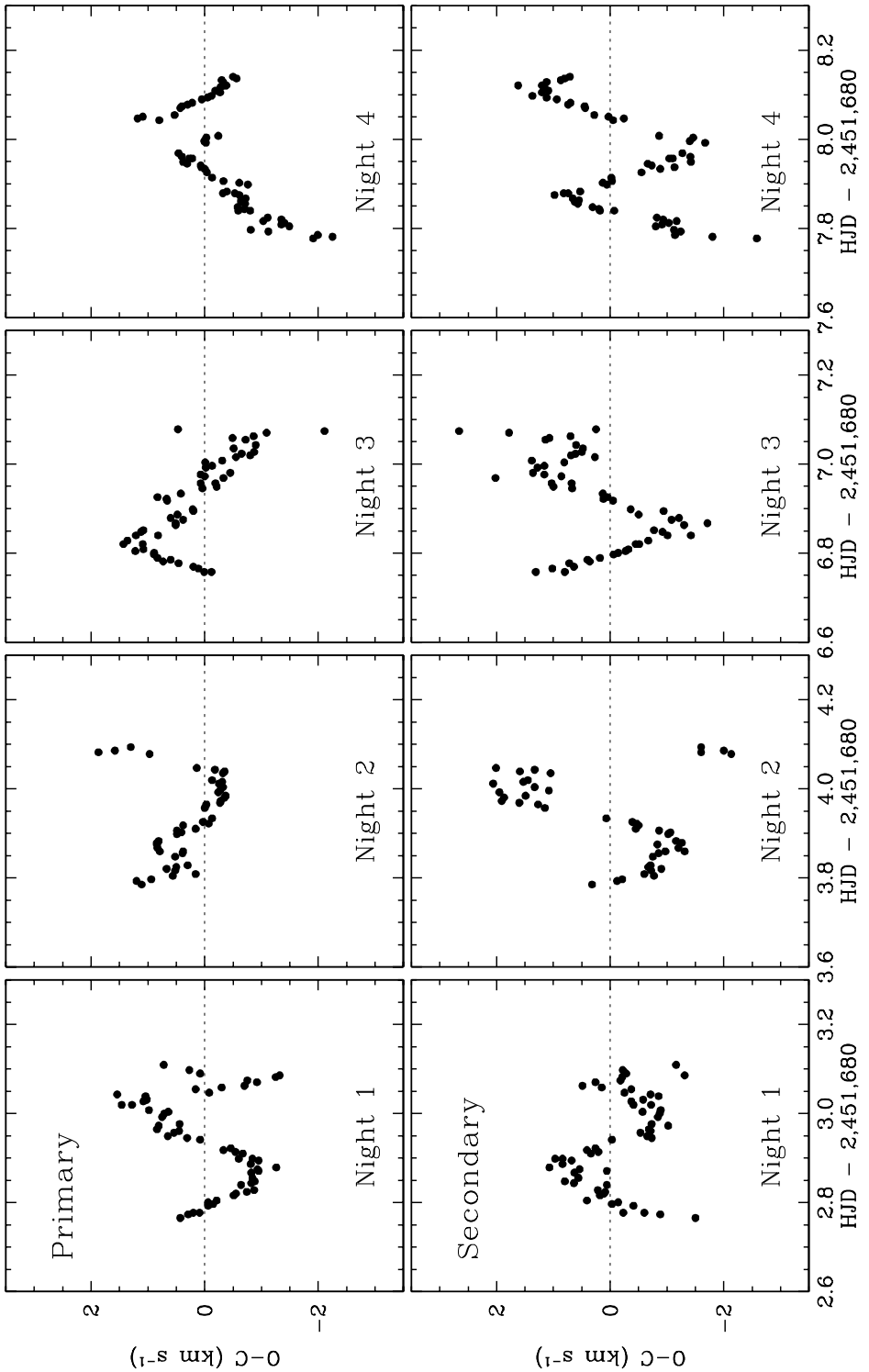

Fig. 3.— Residuals for the individual nights' velocities from SR03.

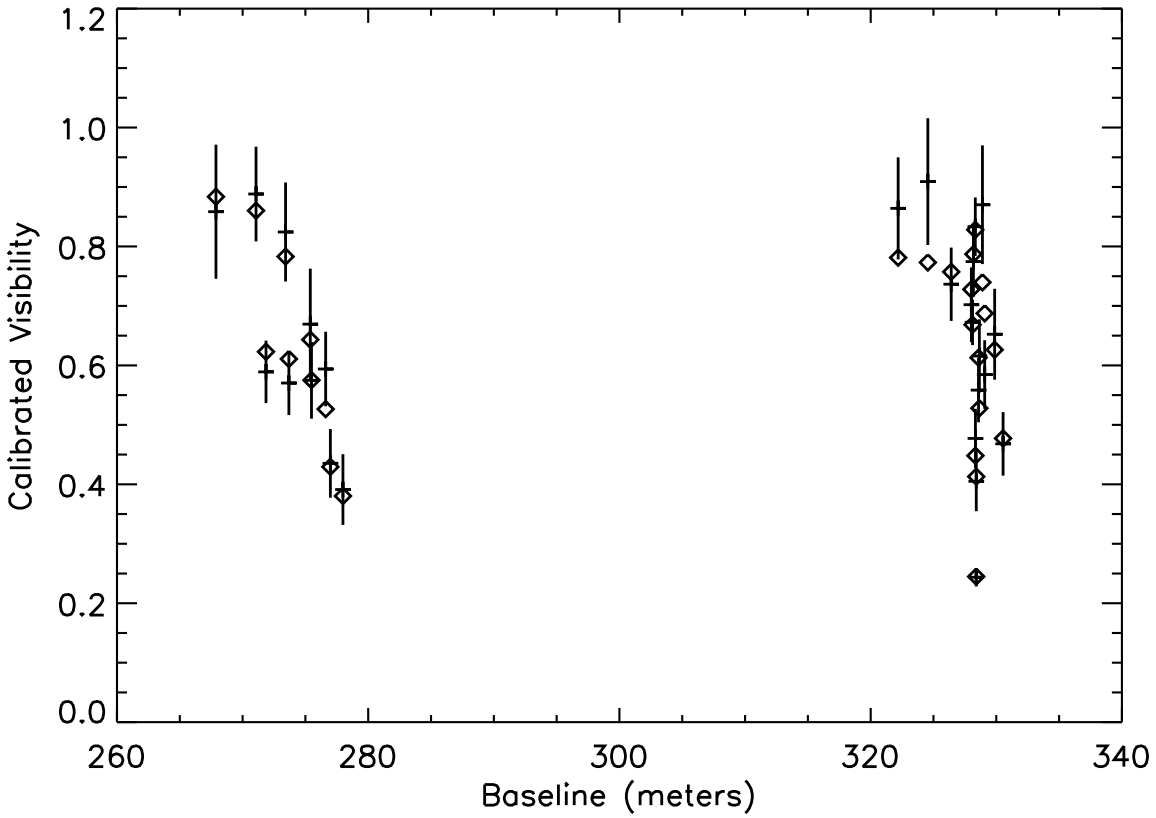

Fig. 4.— Calibrated visibility measurements for σ^2 CrB versus the projected baseline. The plus signs are the calibrated visibilities with vertical error bars, and the diamonds are the calculated visibilities for the best-fit orbit. Table 2 lists the numeric values corresponding to this plot.

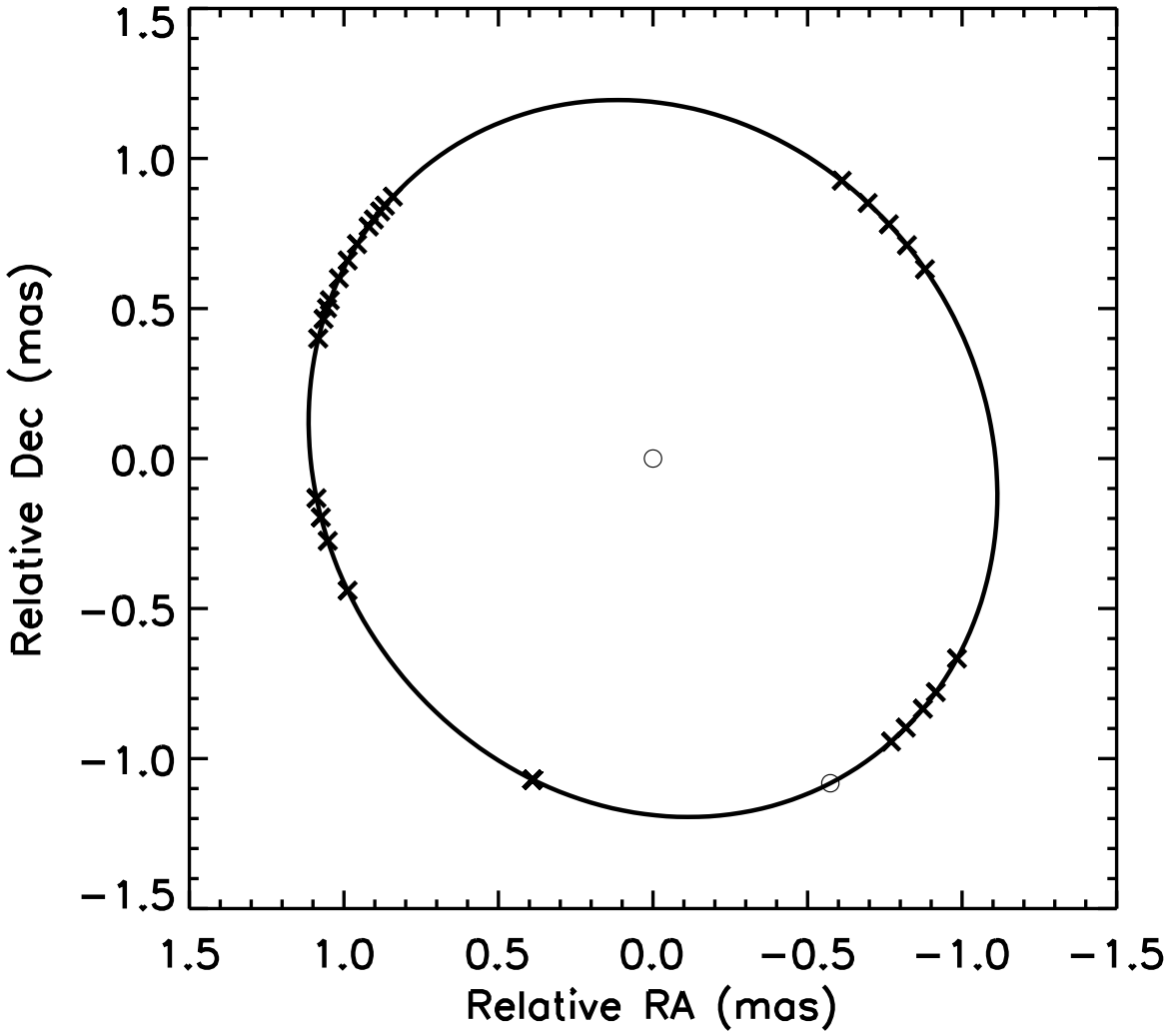

Fig. 5.— The visual orbit of σ^2 CrB. Open circles mark the positions of the two components at the epoch of ascending nodal passage, and the X marks identify the secondary's calculated positions at the epochs of visibility measurement.

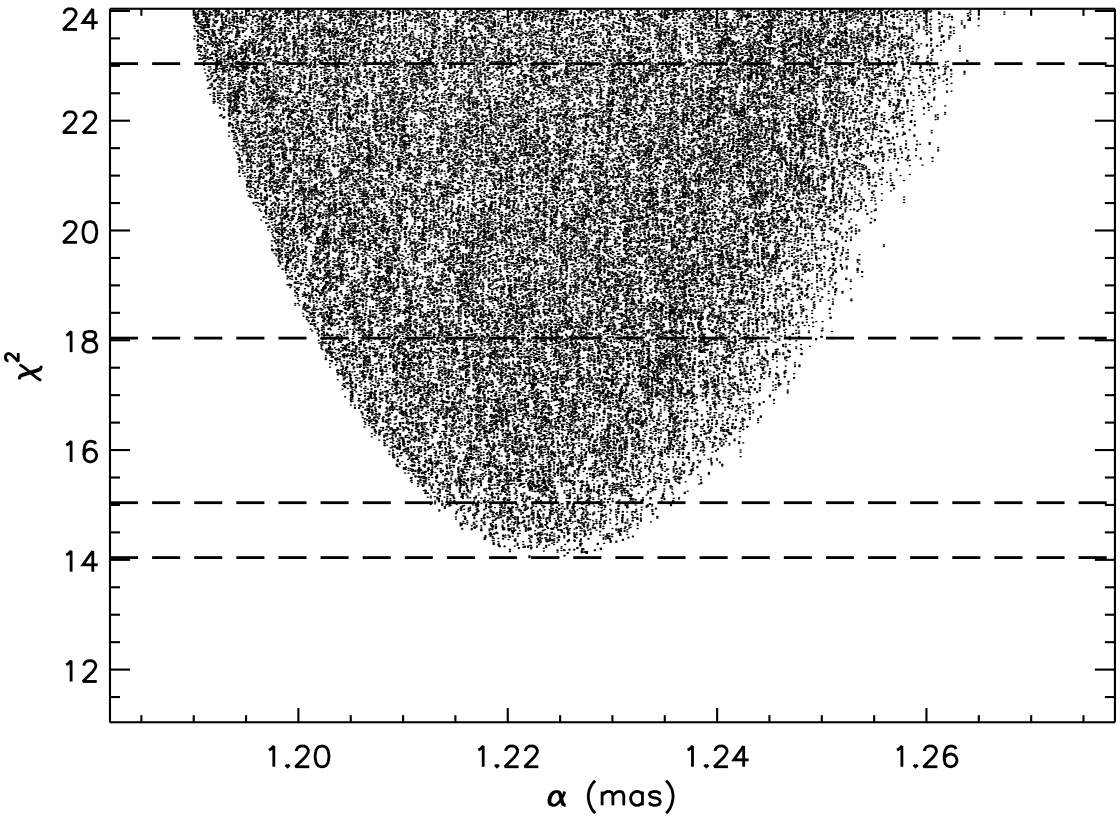

Fig. 6.— χ^2 distribution around the best-fit solution for the angular semimajor axis (α). The bottom dashed line corresponds to the minimum χ^2 value, and the others mark a deviation of 1, 4, and 9 units above the minimum, corresponding to 1, 2, and 3-σ errors.

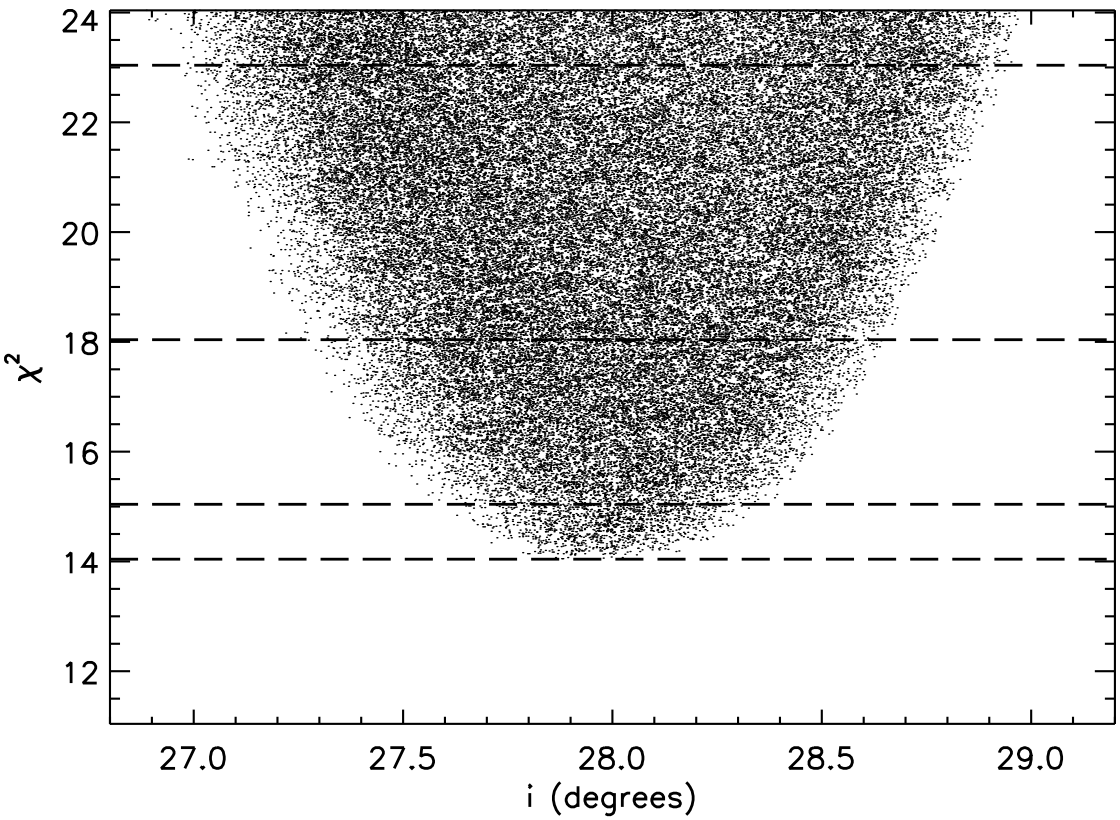

Fig. 7.— Same as Figure 6, but for the orbital inclination (i).

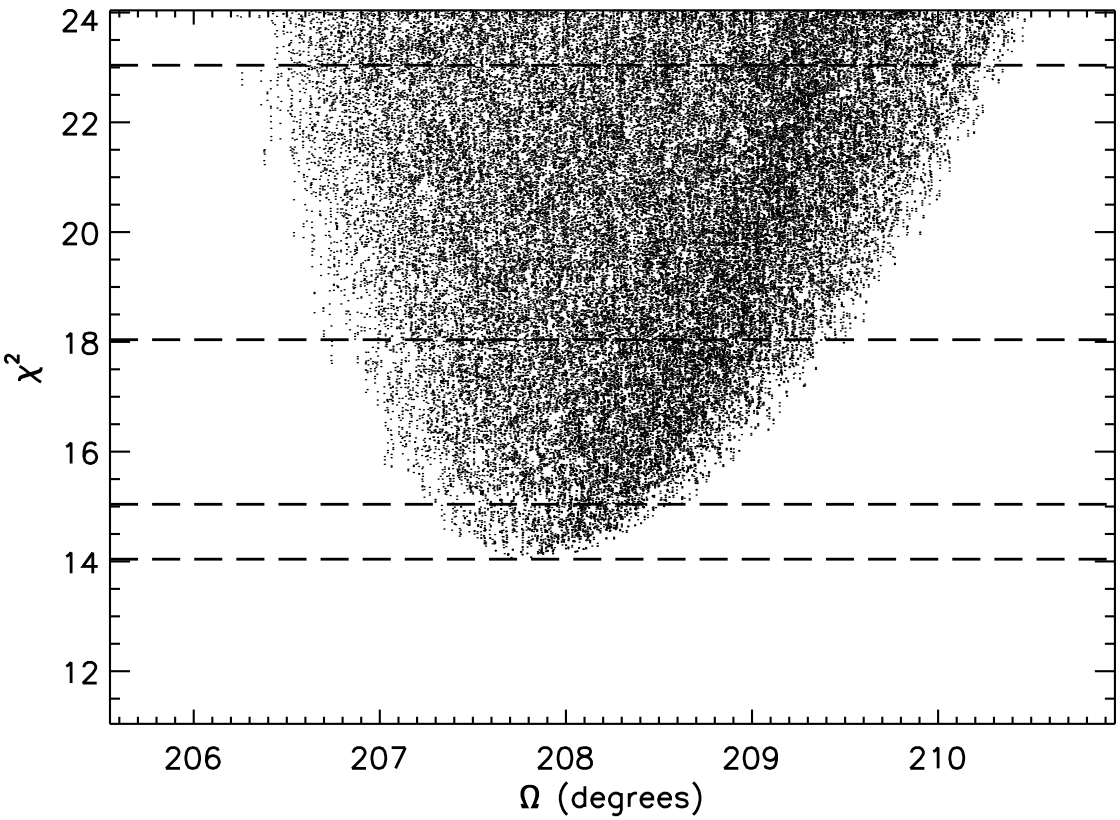

Fig. 8.— Same as Figure 6, but for the longitude of the ascending node (Ω).

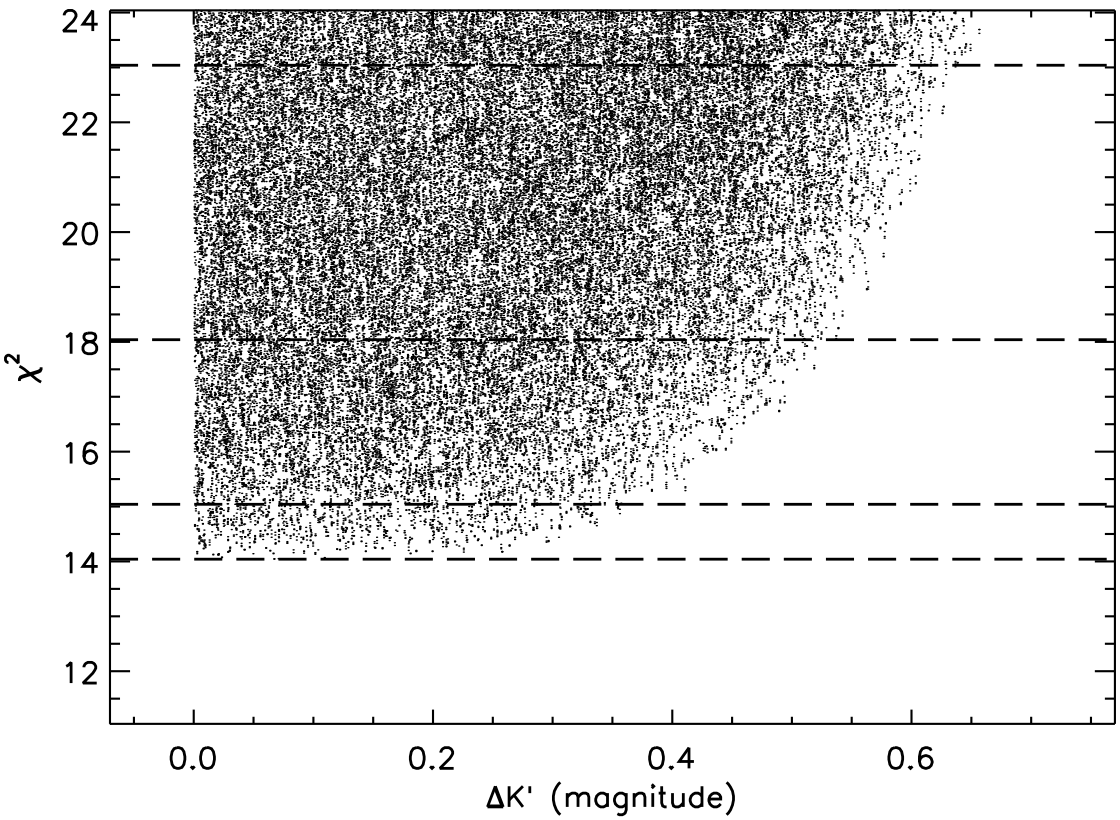

Fig. 9.— Same as Figure 6, but for the K'-band magnitude difference ($\Delta K'$).

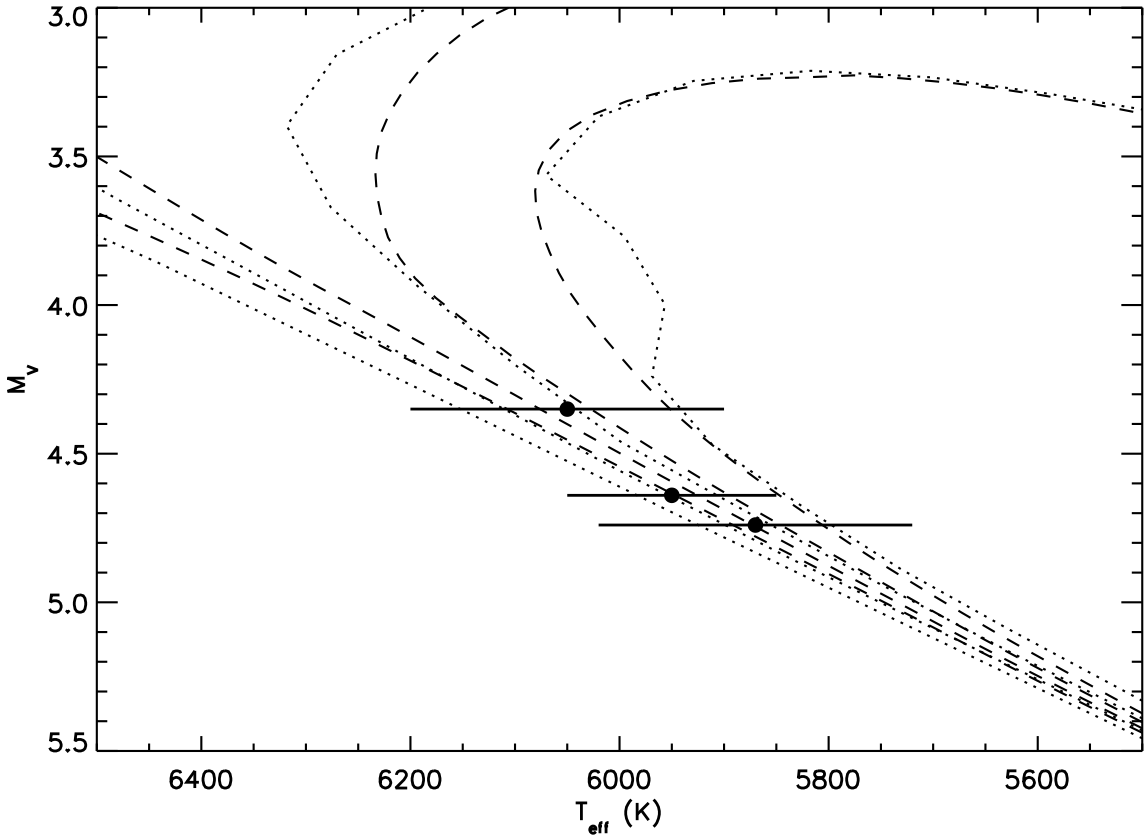

Fig. 10.— The position of the Sun-like components of σ CrB on the H-R diagram. The points from top to bottom are σ^2 CrB primary, σ^1 CrB, and σ^2 CrB secondary. The isochrones are from the Yonsei-Yale (dotted) and Victoria-Regina (dashed models) for 0.5, 1.5, 3.0, and 5.0 Gyr ages (left to right) for solar metallicity stars.

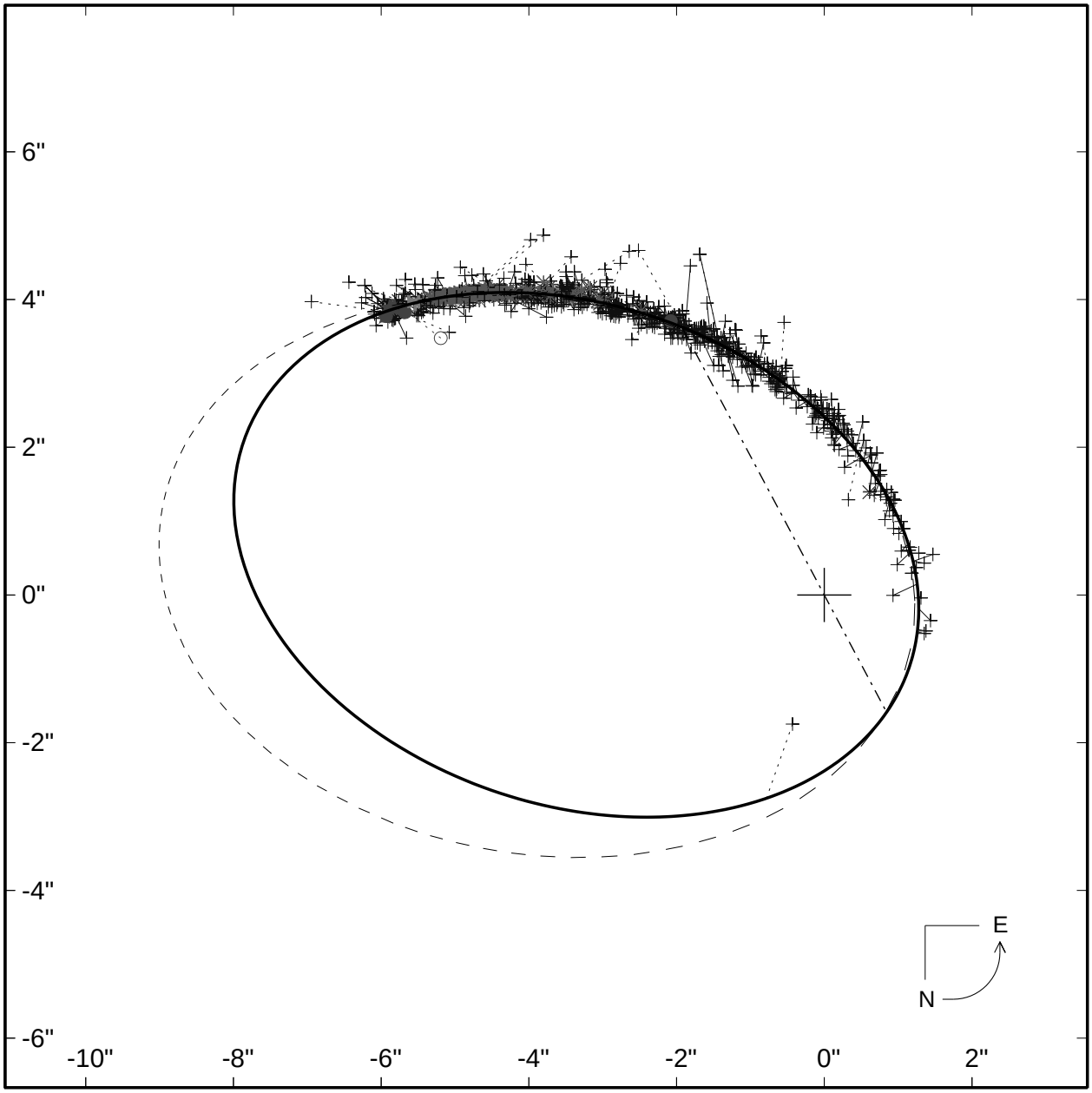

Fig. 11.— The visual orbit of the wider $\sigma^1 - \sigma^2$ CrB (AB) system based on all measures in the WDS. Plus signs indicate micrometric observations, asterisks indicate photographic measures, open circles indicate eyepiece interferometry, and filled circles represent speckle interferometry. The solid curve is our orbit fit and the dashed curve is the Scardia (1979) orbit. $O-C$ lines connect each measure to its predicted position along the orbit. The big plus at the origin indicates the position of the primary and the dot-dash line through it is the line of nodes. Scales are in arcseconds, and the curved arrow at the lower right corner by the north and east direction indicators shows the direction of orbital motion.

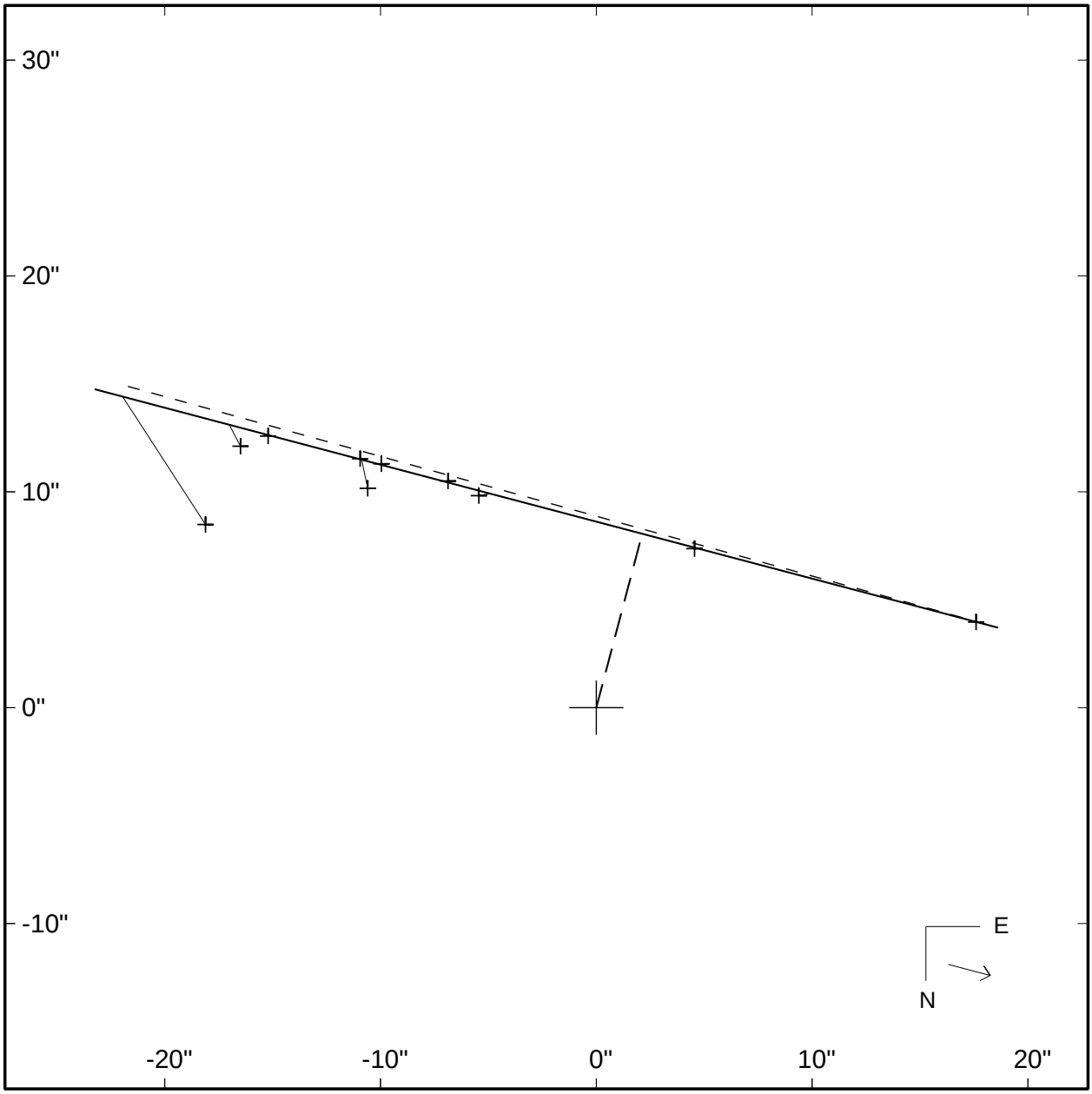

Fig. 12.— Relative separation between σ^2 CrB and ADS 9979C based on 10 resolutions of the pair from 1832 to 1984. Plus signs indicate micrometric observations. $O{-}C$ lines connect each measure to its predicted position along the linear fit (thick solid line). The thick dashed line is the predicted movement based on the differential proper motions. The long dashed line connected to the origin indicates the predicted closest apparent position. The scale is in seconds of arc. An arrow in the lower right corner by the north and east direction indicators shows the direction of motion of the star.

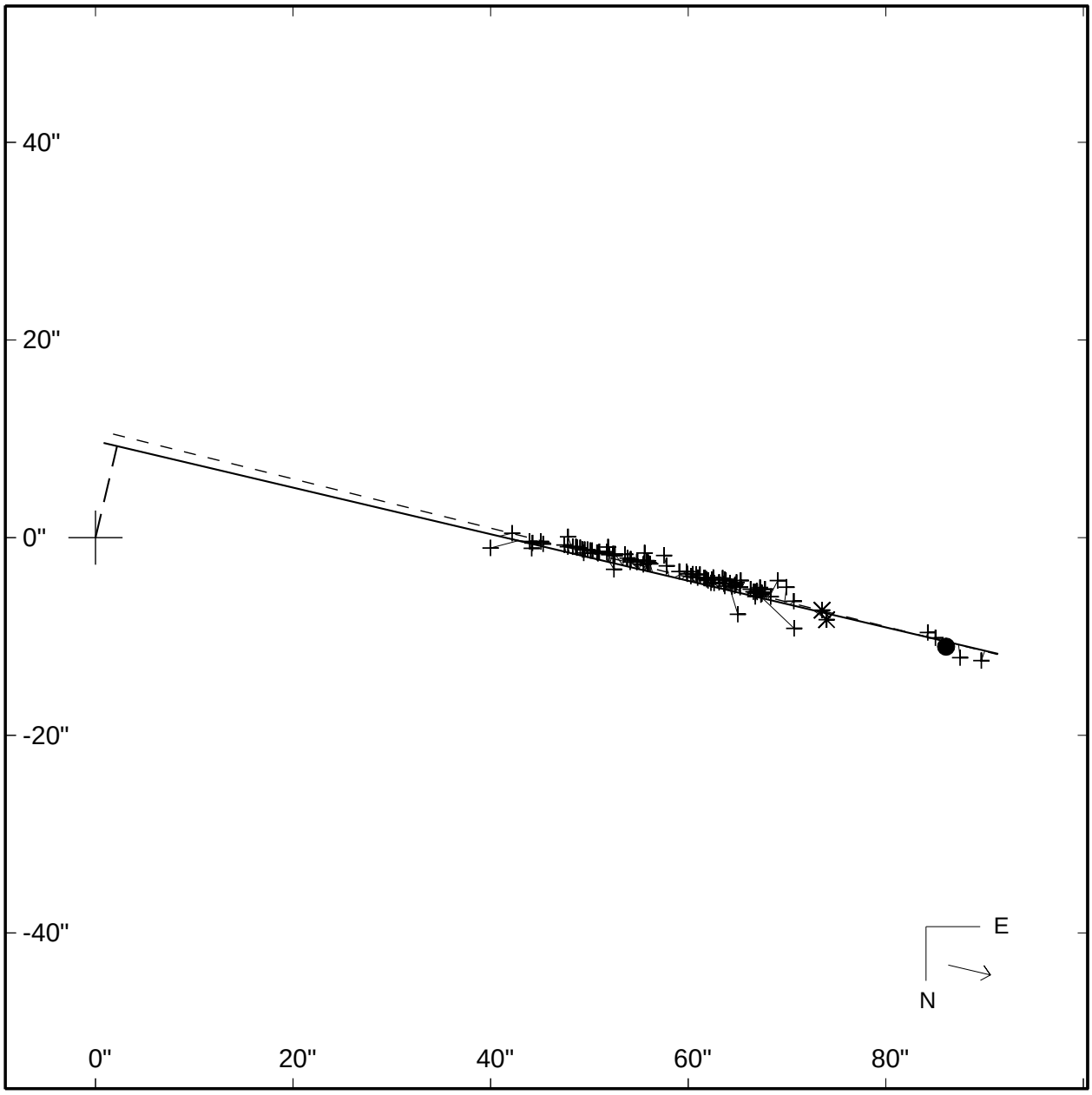

Fig. 13.— Same as Figure 12, but for ADS 9979D based on 106 resolutions of the pair from 1825 to 1996. Asterisks indicate photographic measures and filled circles represent Tycho measures.

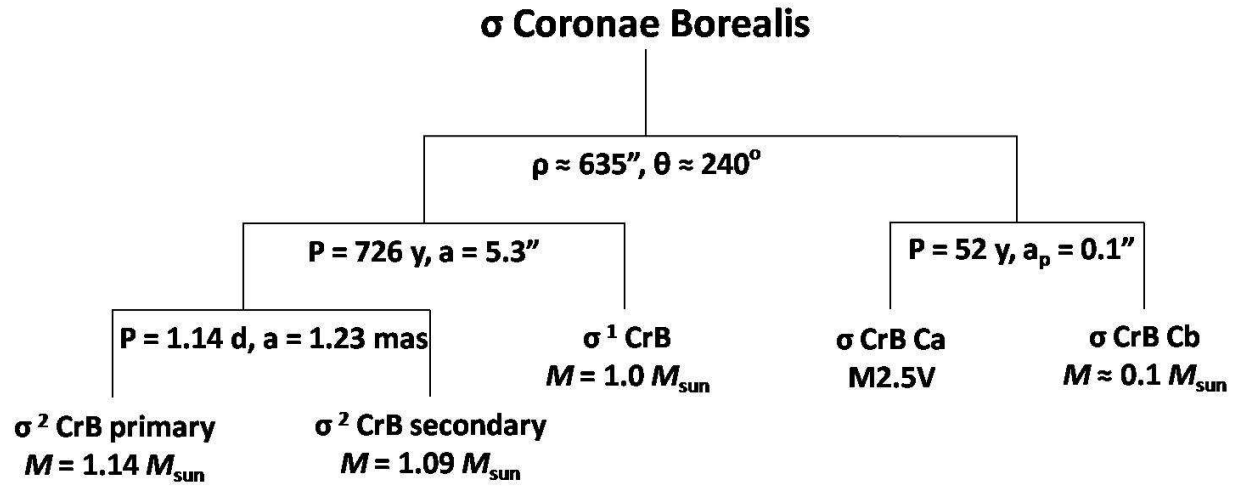

Fig. 14.— Mobile diagram of σ CrB and some of its properties. The Ca-Cb pair is WDS component E, while WDS components C & D are not gravitationally bound to the σ CrB system (see Figures 12 and 13, and text in § 7). a_p for the Ca-Cb pair is the photocentric semimajor axis.